Since January 2020 Elsevier has created a COVID-19 resource centre with free information in English and Mandarin on the novel coronavirus COVID-19. The COVID-19 resource centre is hosted on Elsevier Connect, the company's public news and information website.

Artificial Intelligence In Medicine 134 (2022) 102427

Contents lists available at ScienceDirect

Artificial Intelligence In Medicine

journal homepage: www.elsevier.com/locate/artmed

Research paper

COVID-DSNet: A novel deep convolutional neural network for detection of coronavirus (SARS-CoV-2) cases from CT and Chest X-Ray images

Hatice Catal Reis [a,*], Veysel Turk [b]

[a] Department of Geomatics Engineering, Gumushane University, Gumushane 2900, Turkey
[b] Department of Computer Engineering, University of Harran, Sanliurfa, Turkey

ARTICLE INFO

Keywords:
Chest CT-scan images
Chest X-ray images
COVID-DSNet
Depthwise separable convolution
SARS-CoV-2

ABSTRACT

COVID-19 (SARS-CoV-2), which causes acute respiratory syndrome, is a contagious and deadly disease that has devastating effects on society and human life. COVID-19 can cause serious complications, especially in patients with pre-existing chronic health problems such as diabetes, hypertension, lung cancer, weakened immune systems, and the elderly. The most critical step in the fight against COVID-19 is the rapid diagnosis of infected patients. Computed Tomography (CT), chest X-ray (CXR), and RT-PCR diagnostic kits are frequently used to diagnose the disease. However, due to difficulties such as the inadequacy of RT-PCR test kits and false negative (FN) results in the early stages of the disease, the time-consuming examination of medical images obtained from CT and CXR imaging techniques by specialists/doctors, and the increasing workload on specialists, it is challenging to detect COVID-19. Therefore, researchers have suggested searching for new methods in COVID- 19 detection. In analysis studies with CT and CXR radiography images, it was determined that COVID-19-infected patients experienced abnormalities related to COVID-19.

The anomalies observed here are the primary motivation for artificial intelligence researchers to develop COVID-19 detection applications with deep convolutional neural networks. Here, convolutional neural network-based deep learning algorithms from artificial intelligence technologies with high discrimination capabilities can be considered as an alternative approach in the disease detection process. This study proposes a deep convolutional neural network, COVID-DSNet, to diagnose typical pneumonia (bacterial, viral) and COVID-19 diseases from CT, CXR, hybrid CT + CXR images. In the multi-classification study with the CT dataset, 97.60 % accuracy and 97.60 % sensitivity values were obtained from the COVID-DSNet model, and 100 %, 96.30 %, and 96.58 % sensitivity values were obtained in the detection of typical, common pneumonia and COVID-19, respectively. The proposed model is an economical, practical deep learning network that data scientists can benefit from and develop. Although it is not a definitive solution in disease diagnosis, it may help experts as it produces successful results in detecting pneumonia and COVID-19.

1. Introduction

COVID-19, another strain of SARS-CoV-2 infection, is an enveloped, positive single-stranded RNA virus that can cause severe pneumonia and severe acute respiratory distress in humans, which can be fatal [1,2]. Like other coronaviruses (SARS-CoV and MERS-CoV), COVID-19 consists of four structural proteins: spike (S), envelope (E), membrane (M), and nucleocapsid (N) [3]. The viral envelope's S, E, and M proteins consist of a lipid bilayer, while the N protein holds the RNA genome [3]. Many viruses bind to the cell membrane of the host cells and the receptors of the cells with viral glycoproteins, allowing the viruses to attach to the host cells [4]. The virus attached to the cell infects the host cell. S-glycoprotein is the viral protein responsible for virus entry into host cells [4]. The S- protein is located on the outer surface of the coronavirus and forms spikes on the surface of the virus to infect host cells [5]. The S-glycoprotein is initially closed, where the virus must first become on/activated before it can infect the human cell [6]. The open S-protein enters the cell by binding to the receptor-binding domain (RBD) and the ACE-2 (Angiotensin-converting enzyme 2) receptor located on the surface of respiratory cells in the host cell [7,8]. The S-protein binding to the ACE-2 receptor associates with the plasma membrane, where it undergoes proteolytic cleavage [9,10]. The genetic material

* Corresponding author at: Department of Geomatics Engineering, Gumushane University, Gumushane 2900, Turkey.
E-mail address: hcatal@gumushane.edu.tr (H.C. Reis).

https://doi.org/10.1016/j.artmed.2022.102427
Received 11 May 2022; Received in revised form 7 October 2022; Accepted 13 October 2022
Available online 17 October 2022

(viral RNA) of the virus that enters the cell passes into the cytoplasm, where RNA replication (replication of the SARS-CoV-2 virus occurs entirely in the cytoplasm), transcription (copying DNA to mRNA), and translation (polypeptide synthesis as a result of decoding of the mRNA code with the viral polymerase enzyme) takes place [11]. ACE-2 receptors are found in various human tissues, such as myocardial cells, type II alveolar cells, proximal tubule cells, hepatocytes, and cholangiocytes [12]. When SARS-CoV-2 binds to the ACE-2 receptor of the host cell, it triggers oxidative stress (production of free radicals in large numbers) and excessive inflammatory response (overreaction of the immune system to infection), acute respiratory failure (Acute Respiratory Distress Syndrome-ARDS), lung failure, and cause pneumonia. In the human respiratory system, the oxygen taken from the outside with the help of the nose and mouth comes to the lungs after passing through the pharynx, larynx, and trachea. It comes to the alveoli (air sacs) from the bronchi and bronchioles. The oxygen coming to the alveoli is cleaned and passes into the blood surrounding the alveoli's capillaries. Capillaries distribute blood throughout the body. Carbon dioxide in the contaminated blood comes to the alveoli with the help of capillaries, passes through the bronchi (bronchus, bronchus) and trachea, and goes out using the larynx, pharynx, nose, or mouth. Here, the alveoli must remain open for respiration (oxygen transfer from the alveoli to the capillaries or carbon dioxide transfer from the capillaries to the alveoli) [13]. Atelectasis, which may occur due to causes such as fibrosis (hardening of the lung tissue), pathological fluid accumulation in the alveoli, lung tumors, and respiratory failure, is a respiratory complication resulting from not getting air to the alveoli [13]. In the case of atelectasis, the lung is left without air, and in this case, the respiratory function will not be able to be fulfilled as the alveoli are entirely closed. The alveoli walls are composed of a single layer of epithelial tissue composed of type 1 and type 2 cells [14]. Surfactant, which is secreted by type 2 cells responsible for the surface tension of the alveoli and has a vital function in respiration, prevents the closure of the alveoli by providing surface tension [14]. Pneumonia (pneumonia); is an infection of the lung tissue caused by factors such as viruses, bacteria, and fungi [15]. Pneumonia caused by SARS-CoV-2 causes pulmonary edema complications [16]. There is also air and pathological fluid in the alveoli [16]. The liquid accumulating in the alveoli will prevent the surfactant from performing its duty. In this case, the gas exchange between oxygen and carbon dioxide will decrease, and therefore hypoxemia (type I respiratory failure) [17] will occur.

It will be difficult for infected patients to breathe in the picture that occurs due to hypoxemia. Hypoxemia may also occur as a result of the filling of cells (inflammatory, malignant), pus (pneumonia), blood (pulmonary hemorrhage) in alveoli other than fluid [18]. Lack of oxygen in the blood in the bloodstream type I (hypoxemia) excess carbon dioxide in the blood type II (hypercapnia) refers to respiratory failure [19]. Hypoxemia is the predominant finding of respiratory failure in patients with severe pneumonia due to SARS-CoV-2, while hypercapnia respiratory failure is rare [20]. In the result of pneumonia (pulmonary edema) caused by SARS-CoV-2, foggy structures are seen in the lung density; this unclear image in the lung is called ground-glass opacities (GGO) [21]. GGO does not occur solely as a result of SARS-CoV-2 infection. In the clinical study performed by Valaiyapathi et al. GGO was also observed as a result of acute eosinophilic pneumonia in an 83-year-old male patient [22]. Consolidation is the accumulation of fluid, cells, pus, or blood that interferes with the functioning of the alveoli [23]. In the case of a consolidation, the interstitium, the tissue between the pulmonary alveoli and the capillaries, is affected [24]. In the GGO symptom, bronchial (bronchi) and vascular (vessels) structures are seen, while bronchovascular forms (bronchial vasculature) are not visible in the consolidation area [25]. GGO can also be seen with different findings such as consolidation and interlobular septal thickening [26]. As a result, symptoms of inflammation in the bronchi and alveoli, fibrosis, loss of surfactant, pulmonary edema, and thickening of the capillary wall, respiratory failure (decreased oxygen in the blood or increased carbon dioxide in the blood) can be seen in patients infected with SARS-CoV-2. The lack of effective treatment of SARS-CoV-2 infection has caused difficulties in education, economy, and tourism worldwide, especially in health, due to its rapid transmission and the increasing number of deaths [27,28]. It also has negative effects on human physical and mental health [29]. SARS-CoV-2 virus; can be transmitted through droplets, indirect contact of infected people with surfaces, tools or devices used by infected people, and direct contact with the infected person [30]. SARS-CoV-2 infection primarily affects the respiratory system and the cardiovascular, neuronal, renal, and gastrointestinal [31]. However, it causes serious pathologies in many tissues and organs (heart, brain, kidney, liver, intestine, pancreas), especially in the lung [32]. The disease can cause serious complications in people with medical health problems such as infection, diabetes, liver diseases, cardiovascular diseases (such as coronary artery diseases, peripheral vascular diseases, heart valve diseases), chronic respiratory diseases, cancer (lung cancer, colon cancer, etc.) and it can cause serious complications in patients with weakened immune systems, especially in the elderly [33]. While SARS-CoV-2 infection may occur with mild symptoms in the majority of patients in the early stages in line with clinical findings, or asymptomatic (without any symptoms) in the majority of patients; There are also severe cases that are treated in hospitals, have a high mortality rate, have serious respiratory complications, and with multi-organ failure as a result of the development of an uncontrolled hyper-inflammatory response [34]. It is possible to examine the SARS-CoV-2 disease course in four stages [35]. In the first stage; fever, fatigue, myalgia, dry cough are common symptoms, in the second stage; The majority of SARS-CoV-2 patients show ground glass and consolidative pulmonary opacity on computed tomography, in the third stage; Hypercoagulation (pulmonary embolism/coagulation may occur due to epithelial tissue damage in the intrapulmonary vessels in chronic COVID syndrome) was observed in patients treated in hospitals, finally in the fourth stage; Evidence of multiple organ failure occurs due to an overreaction of the immune system and extreme hypoxemia [35]. In the case infected by the virus, the immune system begins to produce antibodies. The cells responsible for antibody formation are B lymphocytes [36]. An antigenic stimulation activates b lymphocytes by T lymphocytes/cells [36]. Some stimulated B lymphocytes transform into memory B cells, while others transform into plasma cells [37]. Memory B cells do not take an active role against the viral antigen but take an active part when encountering the same antigen [37]. Plasma cells produce antibodies against infection by viral antigen [37]. In a subject with SARS-CoV-2 disease, B lymphocytes produce IgM and IgG antibodies against viral proteins S, E, M, and N [38]. Significant and uncontrolled release of proinflammatory cytokines in patients with SARS-CoV-2 infection causes cytokine storm syndrome and ARDS [39]. As a result of the excessive reaction in the immune system against the viral antigen, it can cause organ damage such as lung, heart, kidney, and as a result, multi-organ failure is observed. In a case with SARS-CoV-2 viral infection, it can lead to heart failure and sudden death in severe cases; myocarditis (heart muscle inflammation), pericarditis (heart membrane inflammation), acute coronary syndrome (heart attack) due to excessive inflammatory response to infection, and symptoms of intravascular coagulation may occur [40]. In a study conducted at the University Hospital in Frankfurt, Germany, cardiac involvement was observed in 78 (78 %) and myocarditis in 60 patients (60 %) of 100 patients (53 males 47 females) who recovered from SARS-CoV-2 infection [41]. In addition, 67 (67 %) of 100 patients experienced the disease at home, and 33 (33 %) were treated in hospital. Viruses must evade the immune system to cause infection/illness in humans. The SARS-CoV-2 virus suppresses the production of interferon (IFN type I and IFN type III) glycoprotein, which stimulates innate immune cells in host cells to fight against microbes or harmful cells that enter the body to prevent recognition by receptors on host cells [38]. Interferon stimulates innate immune cells against viral infection by activating type I and type III IFNs, thus preventing viral protein synthesis and limiting virus infection by generating immune

responses [42]. Infectious viral pathogens have evolved mechanisms to evade the immune system and inhibit the function of IFNs [42]. Excessively increased viral load, IFN inhibition, decreased viral response, and raised pro-inflammatory cytokines may cause worsening of the disease in an infected patient. A study conducted with 50 patients with severe SARS-CoV-2 disease examined the blood taken from the patients, and low interferon activity and chemokine signaling molecules were observed [43]. Therefore, the IFN response is critical in limiting SARS-CoV-2 infection. One of the factors that cause the severe course of the SARS-CoV-2 disease is the viral load. In the study of the researchers on Syrian hamsters, the transmission of SARS-CoV-2 infection, viral nucleocapsid antigen expression, viral load, and histopathological changes due to the use of the mask were examined [44]. Masks (surgical masks, N95, KN95) can prevent transmission or spread of SARS-CoV-2 infection by preventing the transmission of airborne droplets after speaking, coughing, or sneezing [45]. Due to the severe complications of SARS-CoV-2 infection, it was necessary to develop vaccines, antibodies, and antiviral drugs to prevent the disease. The first measure against SARS-CoV-2 infection is prophylactic vaccines that help activate immune cells [46]. Among the types of vaccines against infection; (1) live, inactivated, and attenuated whole virus vaccine (CoronaVac [Sinovac Biotech vaccine] and US20060039926), (2) DNA and mRNA nucleic acid vaccines (mRNA-1273 [Moderna vaccine], BNT162b2 [Pfizer-BioNTech vaccine]), (3) virus-like particle vaccines and recombinant protein vaccines, (4) viral vector vaccines (AZD-1222) [ChAdOx1 nCoV-19 vaccine/Oxford-AstraZeneca], JNJ-78436735 [Johnson & Johnson's Janssen Vaccine], Sputnik V, (5) Other types of vaccines are included, such as the Bacille Calmette-Guerin (BCG) vaccine [46–48]. A high rate of myocarditis could be observed after COVID-19 infection. The research conducted by the Siripanthong et al. [40] determined that the probability of myocarditis after the COVID-19 ID-19 vaccine is low. Therefore, drugs recommended for the treatment of SARS-CoV-2 infection; (1) nucleoside analog drugs such as tenofovir, hydroxychloroquine, chloroquine, remdesivir (2) Lianhua Qingwen (traditional Chinese medicine used in the treatment of influenza viral infection), (3) Mesenchymal stem cell therapy, SARS-CoV-2 plasma therapy, interferon-beta protein therapy, immunotherapy (biological agents), antibody therapy [46]. The genetic material of SARS-CoV-2 entering the host cell passes into the cytoplasm, where RNA replication occurs. Here, while RNA replication occurs in the infected cell, mutations occur due to copying errors during replication. SARS-CoV-2 has undergone various mutations over time, so many variants have emerged. SARS-CoV-2 variants include B.1.1.7 (Alpha), B.1.351 (Beta), P.1 (Gamma), B.1.621/B.1.621.1 (Mu), B.1.617.2 (Delta), B.1.1.529 (Omicron) [49]. Delta and omicron variants are the most dangerous variants of SARS-CoV-2 [50]. Compared to the original virus, the delta variant is distinguished by seven mutations in S-proteins (T19R, Δ157–158, L452R, T478K, D614G, P681R, and D950N) and is more contagious than the original virus [50]. In addition, numerous (26–32) mutations in the S-protein have been found in the Omicron variant [51]. Although it is not specific, the Omicron variant infects 2–3 times faster than the delta [52]. In a study conducted in England, one dose of BNT162b2/ChAdOx1 nCoV-19 vaccine protected against the alpha variant 48.7 % (95 % confidence interval [CI], 45.5 to 51.7), protection against the delta variant was 30.7 % (95 % CI, 25.2 to 35.7); the results of both vaccines were similar. The 2-dose BNT162b2 vaccine had 93.7 % (95 % CI, 91.6 to 95.3) protection against the alpha variant and 88 % (95 % CI, 85.3 to 90.1) against the delta variant; two doses of ChAdOx1 nCoV-19 vaccine had 74.5 % (95 % CI, 68.4 to 79.4) protection against alpha variant and 67.0 % (95 % CI, 61.3 to 71.8) protection against delta variant [53]. According to another study, it was revealed that two doses of the BNT162b2 vaccine prevented 70 % against omicron variant-related hospitalization [52]. Research by Muik et al. [54] shows that two doses of BNT162b2 have a low neutralizing ability against the omicron, so the third dose of BNT162b2 is required to prevent SARS-CoV-2 infection. Another study estimated that natural immunity against re-infection in persons infected with SARS-CoV-2 was conferred with an efficacy of 95.2 % (95 % CI: 94.1–96.0 %) for at least seven months [55]. It is essential to diagnose and isolate the infected patients quickly to limit the spread of the infection in the picture caused by SARS-CoV-2 infection. Reverse transcription-polymerase chain reaction (RT-PCR), IgM-IgG antibody tests, Computed Tomography (CT), and chest X-ray (CXR) medical imaging methods are frequently used in the diagnosis of infection [56]. On the other hand, false negative (FN) results in RT-PCR, IgM-IgG antibody tests in the early stages of the disease, limited test kits, symptoms similar to other diseases such as pneumonia and influenza, RT-PCR as a result of mutations in the SARS-CoV-2 virus The problems that can be experienced in detecting the disease with test kits, the restrictions in health access due to the density experienced in hospitals as a result of the rapid increase in the number of cases, the time-consuming and costly manual examination of the data obtained from CT and CXR medical imaging techniques by experts, the increasing workload on experts, the problems caused by inability of vaccines to completely prevent the disease; has made the SARS-CoV-2 infection deadly, causing the death of millions of people around the world [1,57–59]. Alternative fast and reliable methods are needed to protect from the devastating effect of the infection. Examining images from CT and CXR medical imaging techniques, significant differences were observed between infected (GGO, consolidative pulmonary opacity) and uninfected images [60]. This has been the primary motivation for artificial intelligence researchers. Here, deep convolutional neural network-based deep neural networks, one of the artificial intelligence technologies that can produce successful results in linear or non-linear problems, can be considered an alternative approach in the disease detection process. Artificial intelligence technologies with high processing power (machine learning and deep learning algorithms) are nowadays used in the automatic diagnosis of many diseases such as lung cancer [61], skin cancer [62], brain tumor [63], colon cancer [64], automatic classification of medical images and used in segmentation for COVID-19 detection [65].

Machine learning methods are usually trained with large datasets (input data) in the supervised learning process; then predictions are made (decision making). Machine learning algorithms automatically extract the hidden relationships or patterns between the data and produce highly accurate results in the training process. Ouchicha et al. [66] proposed the CVDNet architecture to detect COVID-19 from chest X-ray images. The architecture consists of two parallel blocks. In architecture, the convolution layer outputs are transmitted from the related block to the other block. Here, the transmitted feature vectors are added to the layer in which they are located. The architecture is developed with the convolutional layer. Sahin [67] proposed a lightweight (11-layer) CNN-based architecture developed with the convolutional layer for detecting COVID-19 from chest X-ray images. Mukherjee et al. [68] proposed a lightweight (9-layer) CNN-based deep neural network developed with a convolutional layer for COVID-19 detection using CT and chest X-ray medical images. Researchers used MobileNet architecture pre-trained with ImageNet for COVID-19 detection from chest X-ray images [69]. The MobileNet architecture was developed with residual networks (MNRSC) in the study. The proposed MNRSC architecture has improved the performance of the underlying MobileNet architecture. The standard MobileNet architecture is enhanced with a depthwise separable convolution layer.

Architectures proposed in the literature for COVID-19 detection research are generally developed with convolutional layers. The depthwise convolution and separable convolution layers can reduce the computational complexity of the architectures proposed here and train the architectures with fewer parameters. Architectures can be developed with additional feature vectors to increase the architectures' performance and prevent the information loss/gradient loss problem that may occur in hierarchical feed forward neural networks. This study proposes COVID-DSNet, a depthwise convolution and separable convolution-based deep convolutional neural network to diagnose normal, bacterial pneumonia, viral pneumonia, COVID-19 diseases in CT, CXR, and

hybrid CT + CXR medical images. The proposed COVID-DSNet architecture is enhanced with heavy use of additional feature vectors and residual networks to avoid the gradient disappearance problem. The proposed model has been compared and analyzed with the modern architectures InceptionResNetV2, InceptionV3, MobileNet, ResNet-101, DenseNet-169, NASNetMobile, EfficientNetB0 algorithms. All architectures were trained with train and validation data under the same conditions, then tested (with test set). The proposed COVID-DSNet architecture within the scope of the study was developed with dense layer (COVID-DSNet + FCC (Fully Connected Layer)) and LSTM (Long Short-Term Memory) layer (COVID-DSNet + LSTM) and compared with all other architectures together with the original architecture. The LSTM layer is a successful and popular solution technique for detecting hidden patterns/information in images and contextual information [70]. In the study, binary and multi-class classification, hybrid CT + CXR (Non-COVID- 19, COVID-19), binary classification was made with medical images. Accuracy, Positive Predictive Value, Sensitivity, F1-score, Cohen's Kappa metrics were used in the performance analysis of the models. The proposed COVID-DSNet model in the multi-classification study with the CT dataset achieved 100 %, 96.36 %, and 97.60 % accuracy in the training, validation, and testing stages. When the empirical results were examined, it was observed that the proposed COVID-DSNet model produced successful results. The proposed model is open to development and economical and has produced successful pneumonia and COVID-19 disease detection results. We acknowledge that medical diagnostic kits, medical imaging techniques, healthcare institutions, and healthcare personnel are essential in detecting COVID-19 disease and preventing infection. The proposed method has been developed to assist experts in accurate and rapid diagnosis. The Flowchart of the study is shown in Fig. 1.

In summary, the contributions of our study can be summarized as follows:

1. An economical, relatively low parameter depthwise convolution, separable convolution-based deep convolutional neural network COVID-DSNet, which can help in the early diagnosis of COVID-19 disease, is proposed.
2. The architecture has been developed by adding the LSTM and dense layers to the classifier layer of the proposed COVID-DSNet architecture. Thus, the performance analysis of the architecture developed with different classifiers was carried out.
3. Comparative performance analysis was carried out with the proposed architectures (COVID-DSNet, COVID-DSNet + FCC, COVID-DSNet + LSTM) with the latest technological approaches InceptionResNetV2, InceptionV3, MobileNet, ResNet-101, DenseNet-169, NASNetMobile, EfficientNetB0.
4. Within the scope of the study of COVID-DSNet and other existing models, the classification process was carried out with a training and verification testing approach. In addition, the K-fold cross-validation method was applied for the performance analysis of the COVID-DSNet architecture.
5. Within the scope of the study, binary (dual classification) multi-class (triple and quadruple classification) classification was made with normal, pneumonia (bacterial, viral), and COVID-19 patient images using CT and chest X-ray medical images. In addition, binary, multi-class classification studies such as viral/COVID-19, bacterial/COVID-19, normal/COVID-19, viral/bacterial/COVID-19, viral + bacterial + normal/COVID-19 were carried out.
6. To create a deep convolutional neural network model with a deep network structure that data scientists can benefit from, with fewer parameters, and which can reduce the cost by reducing the transaction volume in the computation part, and which can help experts/doctors in the fight against SARS-CoV-2 infection, which has turned into a global crisis with negative effects on human, society and socio-economic life.

The study consists of the following titles. In Section 2, a literature review on COVID-19 detection based on deep neural networks. The design details of the proposed COVID-DSNet architecture are given in Section 3. In Section 4, the datasets used in the study, deep learning algorithms, hyperparameters used in deep learning algorithms, K-fold cross-validation, performance metrics, and materials and methods are given. In Section 5, experimental results of classification studies on CT, CXR, and hybrid CT + CXR dataset. Discussion in Section 6 and finally, the conclusion and future work are given in Section 7.

2. Related work

The inadequacy of RT-PCR, IgM-IgG test kits, and the emergence of a significant number of false-negative results in the early stages of the disease have increased the need to develop new methods to detect COVID-19. Here, samples from CT and chest X-ray medical imaging techniques are frequently used to detect lower respiratory tract diseases, especially in artificial intelligence research.

Rapid interpretation of samples from medical imaging techniques; is vital (due to the quick spread of the SARS-CoV-2 virus the extremely high rate of contagion, turning into potentially fatal symptoms).

In this section, a literature study is given. A general summary of the

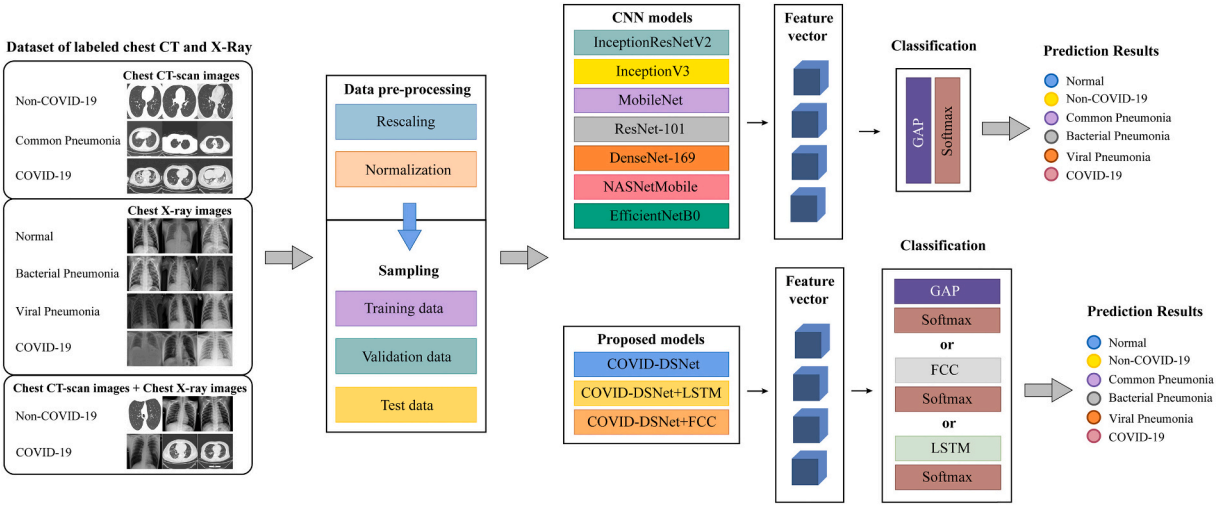

Fig. 1. Flowchart of the study.

literature study is shown in Table 1. The differences observed in CT and chest X-ray images of virus-infected and non-infected patients have increased the interest in using deep convolutional neural network-based architectures with high discrimination power in detecting COVID-19 cases. Gupta et al. [1] proposed the Integrated Stacking InstaCovNet-19 model developed with pre-trained Inception v3, MobileNetV2, ResNet101, NASNet, and Xception models to detect COVID-19 and pneumonia patients using CXR images. The InstaCovNet-19 model was trained and tested with a combined dataset from the COVID-19 Radiography Database and Chest X-ray datasets. InstaCovNet-19 model produced 99.08 % accuracy in triple classification (COVID-19, Pneumonia, Normal) and 99.53 % accuracy in binary classification (COVID-19, Non-COVID-19). Mukherjee et al. [68] proposed a deep convolutional neural network-based architecture for COVID-19 detection from CT and CXR (CT + CXR) images. 96.28 % accuracy, 0.0208 false-negative rates, and 98.08 % AUC value were obtained in the dual classification study on the dataset consisting of 336 COVID-19 cases and 336 Non-COVID-19 cases. Tahir et al. [71] performed a COVID-19, SARS-CoV, or MERS-CoV classification study using the pre-trained deep convolutional neural networks InceptionV3, DenseNet201, SqueezeNet, and ResNet18 architectures. The QU-COVID database created by the authors was used in the study. The QU-COVID database consists of 423 COVID-19, 134 SARS-CoV, and 144 MERS-CoV CXR images from the SARS-CoV-2 family. In the detection study with CXR images; First, the lung sections in the CXR image were determined with the U-Net model. Then segmented images were classified as COVID-19, SARS-CoV, or MERS-CoV with pre-trained deep convolutional neural networks. In the CXR lung segmentation study, the U-Net model produced 93.11 % IoU and 98.21 % accuracy. At the classification stage, plain CXR and segmented CXR images were used. In the study with plain CXR images, the InceptionV3 model was classified as COVID-19, SARS-CoV, MERS-CoV, with 99.5 %, 97 %, and 93.1 % sensitivity; in the study with segmented CXR images, the InceptionV3 model was diagnosed as COVID-19, SARS-CoV, MERS- It produced sensitivity values of 96.9 %, 90.3 %, and 79.7 %, respectively, in CoV classification. On the other hand, Khan et al. [72] proposed using three different pre-trained deep learning algorithms, namely convolutional neural network-based EfficientNetB1, NasNet-Mobile, and MobileNetV2, for the classification of Normal, Lung Opacity, Pneumonia, and COVID-19 infection. The open-access COVID-19 Radiography Database dataset available on the Kaggle site was used in the study. The dataset includes 10,192 normal, 6012 lung opacity, 1345 pneumonia, and 3616 COVID-19 samples. The EfficientNetB1 model has successfully classified normal lung opacity, pneumonia, and COVID-19 with an accuracy of 96.13 %. Chouat et al. [73] used pre-trained deep neural networks InceptionV3, ResNet50, Xception, and VGGNet-19 for COVID-19 detection using CT and CXR images. The study used the COVID-19 Radiography Database dataset, consisting of open-source CT images, COVID-CT, and CXR images. Within the scope of the study, the data augmentation (rotation, flipping, shifting, and scaling) method was applied to improve the performance of deep learning models used in the detection of COVID-19. In the study with CT images, VGGNet-19 (the most successful model) produced 87 % accuracy, and in the study with CXR images, Xception (the most successful model) had 98 % accuracy. Kundu et al. [74] The ET-NET Bagging ensemble classifier model, pre-trained Inception v3, ResNet34, and DenseNet201 deep neural networks are used together, has been proposed to detect COVID-19 from CT images. The SARS-COV-2 Ct-Scan Dataset dataset available on Kaggle was used in the study. The dataset consists of 1249 COVID-19 and 1229 Non-COVID-19 samples. The proposed model produced a successful result with an accuracy value of 97.81 %. Wang et al. [75] proposed a convolutional neural network-based COVID-Net architecture to detect COVID-19 patients from CXR images. In the study, open access 5 (COVID-19 Image Data Collection [76], COVID-19 Chest X-Ray Dataset Initiative, RSNA Pneumonia Detection Challenge dataset, ActualMed COVID-19 Chest X-Ray Dataset Initiative, COVID-19 radiography database) The COVIDx dataset consisting of 13,975 CXR images compiled with the dataset was used. The dataset consists of 3 classes: normal, non-COVID19 (such as viral, bacterial), and COVID-19. VGG-19 and ResNet-50 from deep neural networks were also used with the proposed COVID-Net architecture for disease detection. VGG-19, ResNet-50 and COVID-Net architectures achieved 83.0 %, 90.6 %, 93.3 % accuracy in classification of normal, non-COVID19, COVID-19 disease, respectively. Kumar et al. [77] proposed the SARS-Net model, in which CNN and graph convolutional network (GCN) models are used together to detect COVID-19 from chest x-rays images. Within the scope of the study, Wang et al. [75] the COVIDx dataset introduced in the COVID-NET article was used. The proposed model produced a successful result with an accuracy value of 97.60 %. Abbas et al. [78] developed the DeTraC deep convolutional neural network architecture to detect COVID-19 patients. DeTraC was trained and tested with a dataset of 105 COVID-19, 11 SARS-CoV, and 80 normal CXR images. The DeTraC model produced 93.1 % accuracy and 100 % sensitivity in detecting COVID-19 positive cases. Li et al. [79] proposed the COVNet (ResNet-based architecture) deep learning architecture to differentiate between COVID-19, CAP, and Non-Pneumonia using 4352 CT images (1292 COVID-19, 1735 community-acquired pneumonia (CAP), and 1325 Non-Pneumonia). According to the experimental results, the COVNet model produced 87 % Sensitivity, 92 % Specificity, 95 % AUC in CAP classification, and

Table 1
Deep learning approaches to Covid-19, Pneumonia the diagnosis from CT and Chest X-Rays.

Reference	Method	Classification	Accuracy (%)
Gupta et al. [1]	Integrated Stacking InstaCovNet-19	3-Way (normal, pneumonia, Covid-19) 2-Way (non-Covid-19, Covid-19)	99.08 (3-way), 99.53 (2-way)
Mukherjee et al. [68]	CNN	2-Way (non-Covid-19, Covid-19)	96.28
Tahir et al. [71]	Pretrained deep CNNs (InceptionV3, DenseNet201, SqueezeNet, and ResNet18)	3-Way (SARS-CoV, MERS-CoV, and Covid-19)	99.50 (InceptionV3, Covid-19, sensitivity)
Khan et al. [72]	Pretrained deep CNNs (EfficientNetB1, NasNetMobile, and MobileNetV2)	4-Way (Normal, lung opacity, pneumonia, and Covid-19)	96.13 (EfficientNetB1)
Chouat et al. [73]	Pretrained deep CNNs (InceptionV3, ResNet50, Xception, and VGGNet-19)	2-Way CT (normal, Covid-19) 2-Way CXR (normal, Covid-19)	87.00 (VGGNet-19) 98.00 (Xception)
Kundu et al. [74]	ET-NET Bagging ensemble classifier	2-Way (non-Covid-19, Covid-19)	97.81
Wang et al. [75]	COVID-Net	3-Way (Normal, non-Covid-19 [e.g., viral, bacterial, etc.], and Covid-19)	93.30
Kumar et al. [77]	SARS-Net	3-Way (Normal, non-Covid-19 [e.g., viral, bacterial, etc.], and Covid-19)	97.60
Abbas et al. [78]	DeTraC	3-Way (Normal, SARS-CoV and Covid-19)	93.10
Li et al. [79]	COVNet	3-Way (non-pneumonia, community-acquired pneumonia, and Covid-19)	90.00 (COVID-19, sensitivity)
Mansour et al. [80]	UDL-VAE	Binary and multi classification	Binary – Multi (98.70–99.20)
Ragab et al. [81]	CapsNet	3-Way (normal, pneumonia, and COVID-19)	94

90 % Sensitivity, 96 % Specificity, 96 % AUC in COVID-19 classification. Mansour et al. [80] proposed a new unsupervised deep learning-based variational autoencoder (UDL-VAE) model for detecting COVID-19 from CXR images.

Working process of the proposed UDL-VAE model; (i) adaptive Wiener filtering (AWF) method involved in preprocessing steps to improve the quality of medical images, (ii) AdaGrad and Inception v4 model in the feature extraction process, (iii) consists of the unsupervised variational autoencoder method used in the classification process. The dataset used in the research consists of Normal, COVID-19, SARS, ARDS, and Streptococcus classes. In the UDL-VAE dual classification, an accuracy value of 0.987 was obtained in the multi-classification study. Researchers proposed a capsule neural network (CapsNet)-based model for detecting COVID-19 from CXR images [81]. 5863 CXR medical images were used in the training of the model. The dataset consists of normal, pneumonia, and COVID-19 classes and the proposed CapsNet model gave 94 % accuracy.

3. The proposed COVID-DSNet model

The primary motivation for developing the proposed COVID-DSNet model is the automatic classification/diagnosis of normal, bacterial pneumonia cases, viral pneumonia cases, and Covid-19 cases with datasets consisting of CT and CXR images. In addition, the developed model offers an alternative perspective for solving the vanishing gradient problem in deep neural networks with additional feature vectors and residual networks. In this section, the methodology of the proposed COVID-DSNet architecture is given.

The COVID-DSNet architecture was designed using the TensorFlow Keras deep learning library, basically inspired by the residual networks in the ResNet [82] architecture and the additional feature vectors in the DenseNet [83] architecture. As the depth of the deep neural networks increases, the gradients that update the weights of the neural networks begin to disappear in the backpropagation process. As a result of this situation, training networks will be complex. Here, the residual networks proposed in ResNet architecture and additional feature vectors used in DenseNet architecture are the most effective methods in solving the lost gradient problem. In the ResNet architecture, information from the previous layers is collected in the next layer with the additional layer. DenseNet architecture, on the other hand, unlike ResNet architecture, prior knowledge and later information are combined with the concatenate layer. The architecture is now augmented with networks and additional feature vectors to avoid the gradient lost problem in the proposed COVID-DSNet deep neural network architecture.

The proposed architecture consists of a 224 × 224 × 3 (height, width, depth) input layer, stem layer, DSU blocks that make up the architecture, transition layer, and softmax output layer. Of the blocks that make up the model, the stem block is respectively; consists of a 3 × 3 kernel size value and a Conv2D layer consisting of 48 filters, batch normalization, ReLU activation function, and a 3 × 3 max-pooling layer. 48 (25 × 25 × 48) feature maps were obtained in the output of the stem block. The DSU block, which forms the backbone of the architecture, consists of different filters (e.g., 64, 32, 24, etc.), different kernel sizes (e.g., 3 × 3, 2 × 2, 1 × 1, etc.) parameter values, Conv2D, DepthwiseConv2D, SeparableConv2D layers, batch normalization, ReLU activation function, It consists of UpSampling2D in size 2 × 2 and max-pooling layer in size 1 × 1. The architecture consists of multiple DSU blocks. 24 (25 × 25 × 24) feature maps were obtained from the output of the first DSU block. The Transition layer is now built using the network architecture. The transition layer consists of different filters (e.g., 64, 32, 24 etc.), Conv2D layers with different kernel size (e.g., 3 × 3, 1 × 1) parameter values, batch normalization, ReLU activation function, UpSampling2D in 2 × 2 size and max-pooling layer in 2 × 2 size. There are four transition layers in the architecture. 24 (25 × 25 × 24) attribute maps are obtained from the first transition layer output. The architecture produces predictive values with a fully connected softmax output layer with 2, 3, and 4 possible values. Among the prediction values, the highest value determined the prediction class. The proposed architecture consists of 4.169.897 (Number of trained parameters: 4.166.357) parameters. The network structure of the COVID-DSNet architecture is given in Fig. 2, and the details of the architecture are given in Table 2. Since the model has detailed content, the details given in Table 2 are the summary of the architecture. However, Table 2 is appropriate in terms of providing sufficient information about the proposed model for researchers.

3.1. Development of COVID-DSNet architecture

The proposed COVID-DSNet architecture has been developed with the FCC layer, consisting of many interconnected neurons. The LSTM layer is a successful technique for detecting hidden patterns in images and using contextual information. The network structure of the COVID-DSNet + FCC architecture is given in Fig. 3, and the details of the COVID-DSNet architecture developed with FCC layers are given in Table 3. The network structure of the COVID-DSNet + LSTM architecture is given in Fig. 4, and the details of the COVID-DSNet architecture developed with LSTM layers are given in Table 4.

a) Fully connected layers: The FCC layer is a one-dimensional artificial neural network with many interconnected neurons or nodes. It is often used to optimize predictive results (target results) at the end of the CNN architecture. Information flow between interconnected neurons; input vector, weights between neurons, activation function, and bias values (Formula 1). Here the input vectors contain the result of the previous layer. Hence it represents a feature vector.

$$y = \sigma \sum_{i=1}^{n} w_i x_i + b \tag{1}$$

where; x is the input vector, y is the output vector, w is the weight between neurons, σ is the activation function and b is the bias.

b) LSTM layer: LSTM is an RNN architecture developed by Hochreiter and Schmidhuber [84]. It has been proposed to solve the gradient disappearance problem experienced in architectural RNN architectures. Memory cells, which form the decision mechanisms of the LSTM architecture, are used to solve the gradient disappearance problem. Memory cells decide which relevant contextual information must be deleted or which to retain/store. Here, the decision mechanisms of memory cells consist of gates. Gates consist of the sigmoid (converts inputs to ranges of 0–1 values) and dot product. Each memory cell consists of input, forget, and output ports (Fig. 5). The entrance gate updates the Cell State (the unit responsible for carrying information in the cell) and decides which previous or current information to keep due to the sigmoid process. The forget gate determines which data to delete (unimportant) or which information to support (necessary) from the login. The exit gate decides what information goes into the next cell. At the output gate, the information coming from the Cell State is multiplied by the vector after passing through the tanh function, the previous information, and the current information through the sigmoid function, and the obtained features/information are used in the next cell's input, or the received information is given to the output layer.

Mathematical operations in LSTM architecture:

$$f_t = \sigma\left(W_f x_t + U_f h_{t-1} + b_f\right) \tag{2}$$

$$i_t = \sigma(W_i x_t + U_i h_{t-1} + b_i) \tag{3}$$

$$\check{c}_t = tanh(W_c x_t + U_c h_{t-1} + b_c) \tag{4}$$

$$c_t = f_t \odot c_{t-1} + i_t \odot \check{c}_t \tag{5}$$

$$o_t = \sigma(W_o x_t + U_o h_{t-1} + b_o) \tag{6}$$

$$h_t = o_t \odot tanh\,(c_t) \tag{7}$$

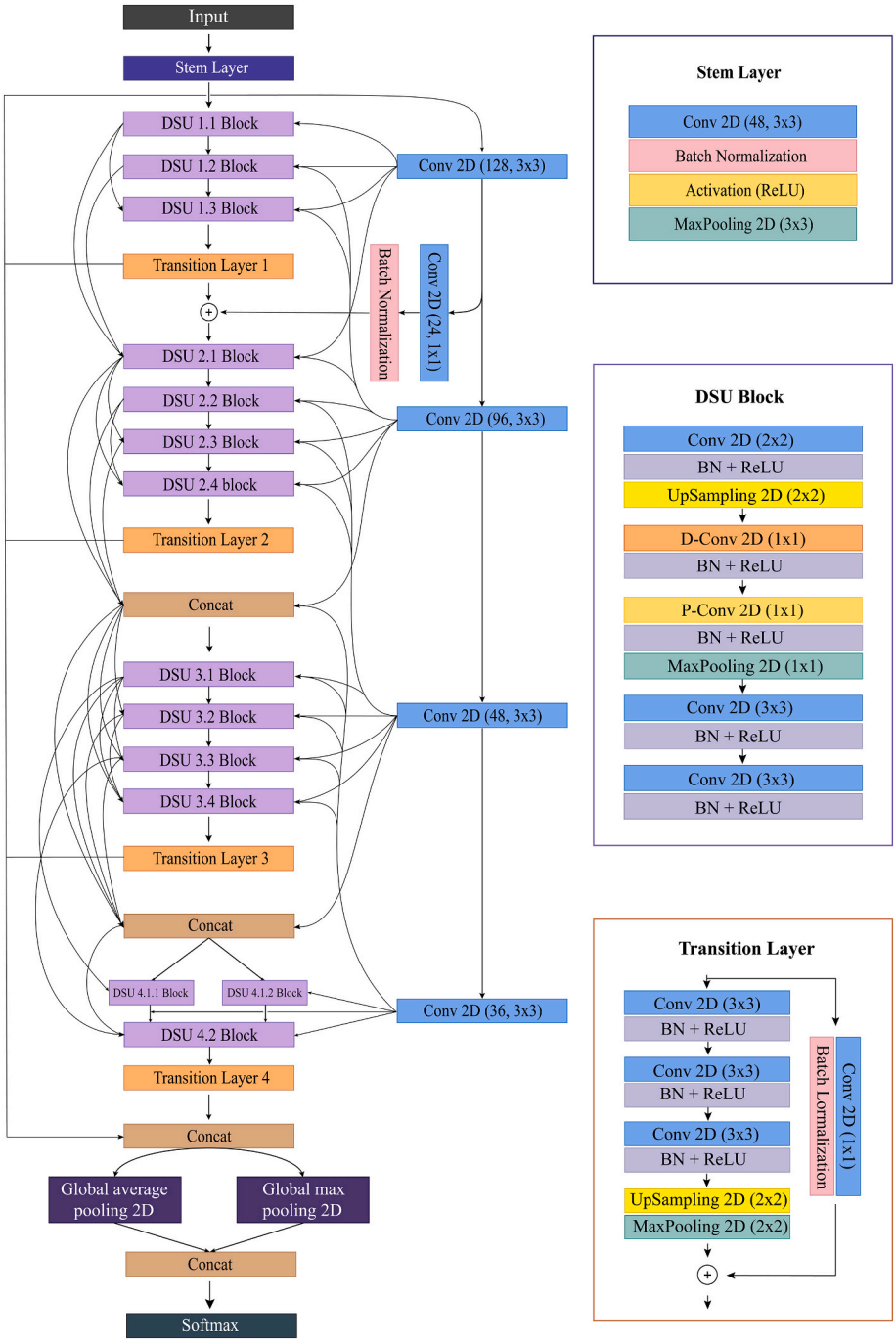

Fig. 2. The architecture of the proposed COVID-DSNet algorithm.

where; f_t is the forget gate, i_t is the input or update gate, o_t is the output gate, σ is the sigmoid function, W_f, W_i, W_o, W_c are the weight matrices of the forget, input, output gate, and cell state, respectively, b_f, b_i, b_o, b_c are the bias values of forgetting, input, output gate, and cell state respectively, x_t is the input vector, U are vectors of size n × n (matrix), c_t and c_{t-1} are cell states at time t and t-1 (cell state), h_t is the hidden state, $\tilde{c}_t$ shows cell input activation vector, and finally ⊙ shows element-based vector multiplication.

3.2. Components of the proposed model

Details of the main components of the proposed model, convolutional layers, separable convolution layer, depthwise convolution layer, activation function, pooling, batch normalization, and dropout are given below.

a) Convolutional layers, depthwise and separable convolution: The convolutional layer, one of the essential functions of the convolutional neural network structure, is used to detect feature vectors from input images. In addition, convolutional layers apply filters to feature maps on input images. The mathematical output of the convolution layer is given in formula 8. The use of multiple convolution layers in deep convolutional neural network architectures causes an increase in the number of parameters, processing power, and cost [85]. In case of an increase in the number of convolution layers during the model's development process, the input data should also increase for the model to be trained efficiently. Here, depthwise separable convolution, a promising

Table 2
The detailed structure of the proposed COVID-DSNet.

Stages	Layers[a]	Output shape (height × width × depth)
Input image	Input layer	224 × 224 × 3
Stem layer	Conv2D (48) @3 × 3 &3 × 3 + BN + ReLU	75 × 75 × 48
	MaxPooling2D (3 × 3)	25 × 25 × 48
DSU block and TL layer	3 × DSU Block (24, 32, 64,128, 24) @1 × 1||2 × 2||3 × 3 &1 × 1||2 × 2	25 × 25 × 368
	TL (64, 32, 24, 24) @1 × 1||3 × 3 &1 × 1	25 × 25 × 24
	4 × DSU Block (12, 16, 32, 64, 12) @1 × 1|| 2 × 2||3 × 3 &1 × 1||2 × 2	25 × 25 × 916
	TL (32, 16, 12, 12) @1 × 1||3 × 3 &1 × 1	25 × 25 × 12
	5 × DSU Block (6, 8, 16, 32, 6) @1 × 1||2 × 2||3 × 3 &1 × 1||2 × 2	25 × 25 × 5400
	TL (24, 18, 14, 14) @1 × 1||3 × 3 &1 × 1	25 × 25 × 14
	4 × DSU Block (4, 6, 8, 16, 4) @1 × 1||2 × 2||3 × 3 &1 × 1||2 × 2	25 × 25 × 12632
	TL (12, 8, 6, 6) @1 × 1||3 × 3 &1 × 1	25 × 25 × 6
	Concatenate	25 × 25 × 104
	GlobalMaxPooling2D, GlobalAveragePooling2D	104, 104
	Concatenate	208
Classifier	FullyConnected (2||3||4) + Softmax	2||3||4

[a] The value after the "@" is the kernel size value. "||" or conjunction. "&" is strides value. TL: Transition layer BN: Batch normalization.

technology, can be used as it uses fewer parameters than the standard convolution layer and reduces the processing volume in the calculation part. Depthwise separable convolution has been implemented in the MobileNet architecture and has produced successful results [85]. Depthwise convolution, separable convolution, and standard convolution study methodology are given in Fig. 6.

$$y_n = \sigma_n(W_n\, x_n + b_n) \tag{8}$$

where; σ_n is a nonlinear activation function, W_n is the convolution kernel, x_n is a vector of input to the node n, b_n is denoted the bias parameter.

Depthwise separable convolution is a depth-wise convolution that follows point-wise convolution. Depthwise convolution is defined as follows.

$$y_{dc} = \sum_{i}^{M} I_i * f_i \tag{9}$$

where; y_{dc} depth-wise convolution shows the result, I_i indicates the channel of the input vector I of channel i., and f_i the filter of channel i. After the Depthwise separable convolution operation is completed, the result obtained is transferred to the Pointwise convolution operation. Pointwise convolution is defined as follows.

$$y_{pc} = \sum_{c}^{N} y_{dc} * f_{1\times1} \tag{10}$$

where; y_{pc} point-wise convolution output, $f_{1\times1}$ 1 × 1 size convolution filter.

Standard convolution processing cost is calculated as $W_K * H_K * C_{in} * C_{out}$ [85]. As a result of this situation, the depthwise separable convolution standard convolution cost ratio is calculated as follows [85].

$$\frac{N_{k_{DC}} + N_{k_{PC}}}{N_{k_{SC}}} = \frac{W_K * H_K * C_{inter} + C_{inter} * C_{out}}{W_K * H_K * C_{in} * C_{out}} = \frac{1}{C_{in}} + \frac{1}{W_K * H_K} \tag{11}$$

where; W, H, C_{in}, C_{out}, C_{inter} are width, height, number of input channels, number of output channels and intermediate channels respectively. $N_{k_{DC}}$, $N_{k_{PC}}$, $N_{k_{SC}}$ are depthwise convolution kernel size, pointwise convolution kernel size, and standard convolution kernel size, respectively.

The operation in formula 11 shows that the cost of depthwise separable convolution is less than the standard convolution.

b) UpSampling layer: It is the process of resizing the input images in high resolution. The UpSampling layer improves image quality and

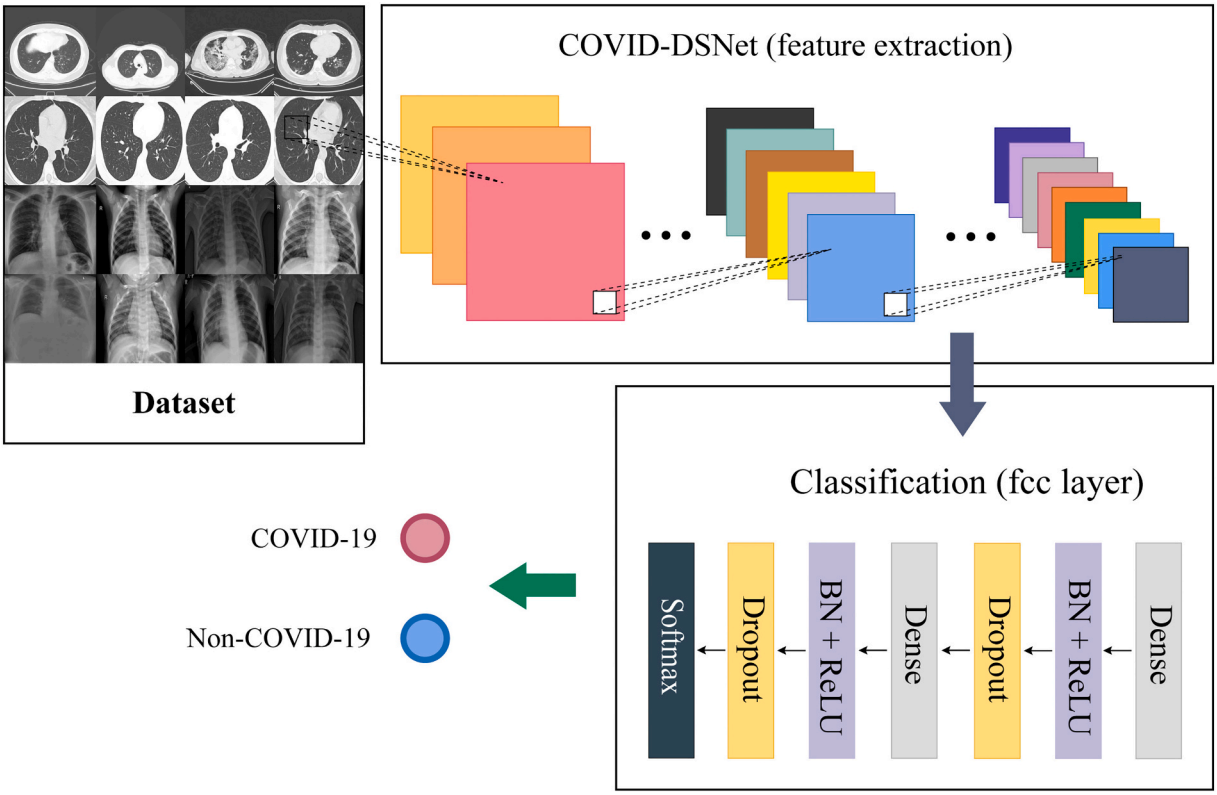

Fig. 3. The architecture of the proposed COVID-DSNet + FCC algorithm.

Table 3
The detailed structure of the proposed COVID-DSNet + FCC.

Stages	Layers[a]	Output shape (height × width × depth)
Input image	Input Layer	224 × 224 × 3
Stem layer	Conv2D (48) @3 × 3 &3 × 3 + BN + ReLU	75 × 75 × 48
	MaxPooling2D (3 × 3)	25 × 25 × 48
DSU block and TL layer	3 × DSU Block (24, 32, 64,128, 24) @1 × 1||2 × 2||3 × 3 &1 × 1||2 × 2	25 × 25 × 368
	TL (64, 32, 24, 24) @1 × 1||3 × 3 &1 × 1	25 × 25 × 24
	4 × DSU Block (12, 16, 32, 64, 12) @1 × 1||2 × 2||3 × 3 &1 × 1||2 × 2	25 × 25 × 916
	TL (32, 16, 12, 12) @1 × 1||3 × 3 &1 × 1	25 × 25 × 12
	5 × DSU Block (6, 8, 16, 32, 6) @1 × 1||2 × 2||3 × 3 &1 × 1||2 × 2	25 × 25 × 5400
	TL (24, 18, 14, 14) @1 × 1||3 × 3 &1 × 1	25 × 25 × 14
	4 × DSU Block (4, 6, 8, 16, 4) @1 × 1||2 × 2||3 × 3 &1 × 1||2 × 2	25 × 25 × 12632
	TL (12, 8, 6, 6) @1 × 1||3 × 3 &1 × 1	25 × 25 × 6
	Concatenate	25 × 25 × 104
	GlobalMaxPooling2D, GlobalAveragePooling2D	104, 104
	Concatenate	208
FullyConnected Classifier	FullyConnected (256) + BN + ReLU	256
	Dropout(rate = 0.2)	256
	FullyConnected (128) + BN + ReLU	128
	Dropout(rate = 0.2)	128
	FullyConnected (2||3||4) + Softmax	2||3||4

[a] The value after the "@" is the kernel size value. "||" or conjunction. "&" is strides value. TL: Transition layer BN: Batch normalization.

reduces noise in images.

c) Activation function: It is a proposed technology to help artificial neural networks learn complex information in data or reveal hidden patterns in data. ReLU and Softmax activation functions were used in the proposed architecture within the scope of the study.

d) Softmax: The softmax function, generally used in the output layer

Table 4
The detailed structure of the proposed COVID-DSNet + LSTM.

Stages	Layers[a]	Output shape (height × width × depth)
Input image	Input layer	224 × 224 × 3
Stem layer	Conv2D (48) @3 × 3 &3 × 3 + BN + ReLU	75 × 75 × 48
	MaxPooling2D (3 × 3)	25 × 25 × 48
DSU block and TL layer	3 × DSU Block (24, 32, 64,128, 24) @1 × 1||2 × 2||3 × 3 &1 × 1||2 × 2	25 × 25 × 368
	TL (64, 32, 24, 24) @1 × 1||3 × 3 &1 × 1	25 × 25 × 24
	4 × DSU Block (12, 16, 32, 64, 12) @1 × 1||2 × 2||3 × 3 &1 × 1||2 × 2	25 × 25 × 916
	TL (32, 16, 12, 12) @1 × 1||3 × 3 &1 × 1	25 × 25 × 12
	5 × DSU Block (6, 8, 16, 32, 6) @1 × 1||2 × 2||3 × 3 &1 × 1||2 × 2	25 × 25 × 5400
	TL (24, 18, 14, 14) @1 × 1||3 × 3 &1 × 1	25 × 25 × 14
	4 × DSU Block (4, 6, 8, 16, 4) @1 × 1||2 × 2||3 × 3 &1 × 1||2 × 2	25 × 25 × 12632
	TL (12, 8, 6, 6) @1 × 1||3 × 3 &1 × 1	25 × 25 × 6
	Concatenate	25 × 25 × 104
FullyConnected Classifier	TimeDistributed (Flatten)	25 × 2600
	LSTM (256) + BN + ReLU	25 × 256
	Dropout(rate = 0.2)	25 × 256
	LSTM (128) + BN + ReLU	25 × 128
	Dropout(rate = 0.2)	25 × 128
	LSTM (64) + BN + ReLU	64
	Dropout(rate = 0.2)	64
	FullyConnected (2||3||4) + Softmax	2||3||4

[a] The value after the "@" is the kernel size value. "||" or conjunction. "&" is strides value. TL: Transition layer BN: Batch normalization.

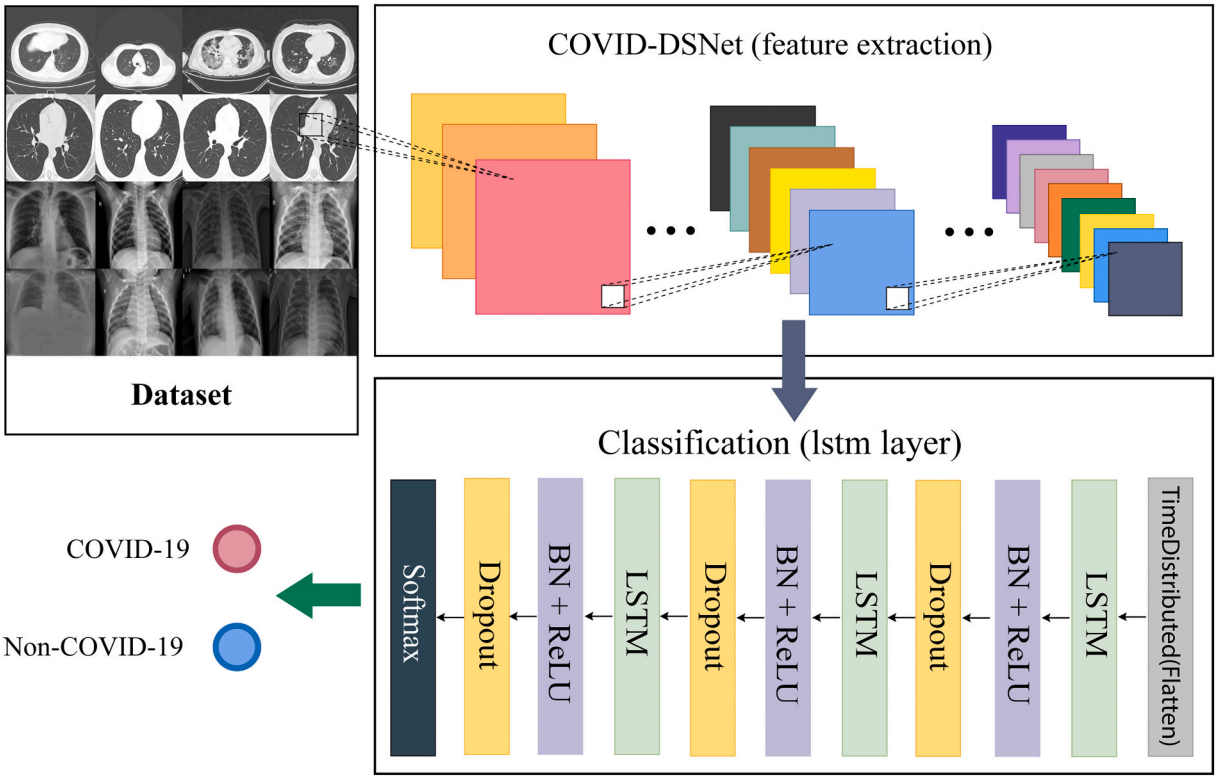

Fig. 4. The architecture of the proposed COVID-DSNet + LSTM algorithm.

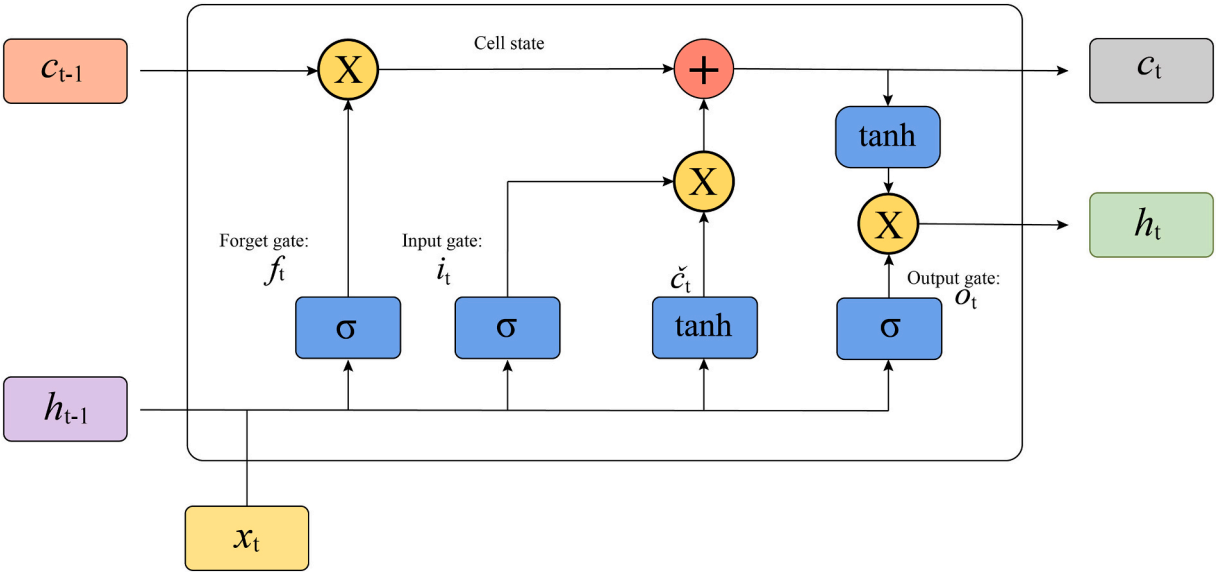

Fig. 5. Architecture of the LSTM algorithm.

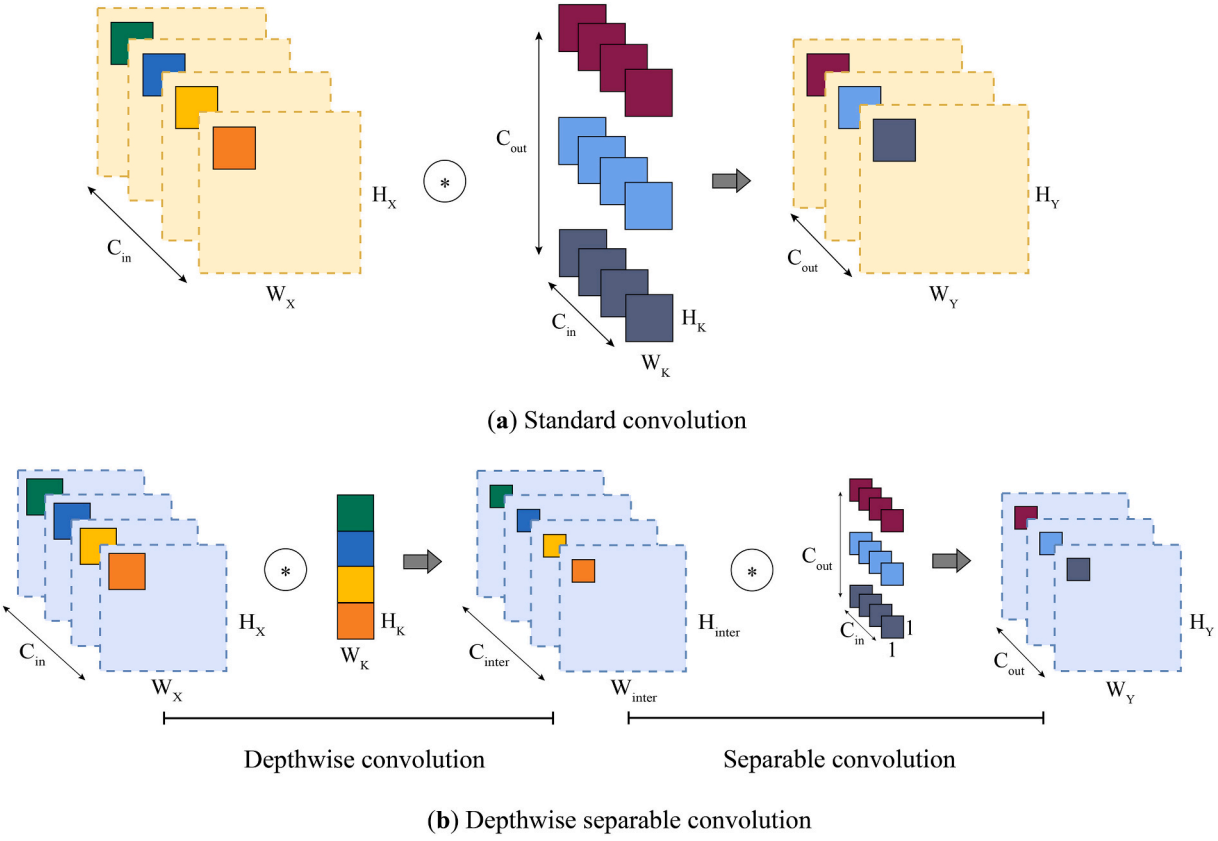

Fig. 6. The working principle of depthwise convolution, separable convolution and standard convolution.

of architectures, generalizes the logistic function used in multi-classification problems to multiple dimensions. The mathematical output of the softmax function is as follows.

$$\text{softmax}\ (x_i) = \frac{e^{x_i}}{\sum_{j=1}^{n} e^{x_j}} \tag{12}$$

where; x is the input vector, x_i is the zero, positive or negative elements of the input vector, e is the exponential function, n is the number of classes of the multi-classifier, $\sum_{j=1}^{n} e^{x_j}$ indicates the normalization term. The normalization term transforms the sum of the output values of the function to be 1, and also brings each output value into the range of 0–1.

e) Rectified Linear Unit (ReLU): ReLU is a nonlinear function frequently used in convolutional layers and middleware. The function produces 0 for negative values and zero and positive values linear. The mathematical output of the ReLU function is as follows.

$$g(x) = max\,(0, x) = \begin{cases} 0, x < 0 \\ 1, x \geq 0 \end{cases} \quad (13)$$

f) Pooling layers: It is frequently used in deep convolutional neural networks to reduce the number of parameters and computational costs in deep neural networks. In the proposed architecture within the scope of the study, max pooling, global max pooling, and global average pooling were used.

g) Batch normalization: The normalization process is applied between layers of neural networks to make deep convolutional neural networks faster and more stable.

h) Dropout: It is the process of ignoring randomly selected neurons according to the threshold value determined in artificial neural networks. It is one of the methods used to prevent excessive learning in the training phase of artificial neural networks. Within the scope of the study, the dropout layer with a threshold value of 0.2 was used in the COVID-DSNet + FCC and COVID-DSNet + LSTM architectures.

i) Flatten: The purpose of this layer is to flatten the input vectors (feature matrix). For example, it converts two-dimensional n × n input vectors to one-dimensional n × 1 vectors. Within the scope of the study, flatten layer was used in the COVID-DSNet + LSTM architecture.

j) Add layer: Take two vectors of the same dimension into a tensor list, then return a single tensor.

k) Concatenate layer: Returns a single tensor by combining all entries of a tensor list with the same dimensions.

3.3. Implementation details

Datasets consisting of CT, CXR, and CT + CXR medical images are divided into 70 % training (10 % of training dataset for validation dataset) and 30 % test dataset. The testing process was carried out during the training with the validation dataset trained with the proposed COVID-DSNet architecture training dataset. After the training process was completed, the model's performance was measured with the test dataset. The man optimization function and the minimum learning rate value of 1e-06 are used in the proposed model. The learning rate was reduced during the model's training when the learning stagnated for a while. If the validation loss value did not decrease during the 2 (patience = 2) cycles during the model's training process, the learning rate value was reduced by 0.5 (factor = 0.5). The new learning rate value is calculated according to formula 14. The loss function used in the proposed model is categorical cross-entropy. The man optimization function is one of the most effective methods to reduce cross-entropy loss and for gradient descent optimization. The cross-entropy loss measures the difference between the predicted value and the true value. The cross-entropy loss increases as the predicted value move away from the true value. Gradient descent optimization is a popular method used to minimize the error value during model training. The proposed model is trained with a training and validation dataset for 50 iterations. A feature/weight vector was obtained at the end of each cycle, but the vector with the lowest validation loss value according to the "mode" parameter was recorded. Performance analysis was carried out with the weight vector test dataset obtained due to the training. The pseudocode of the proposed architecture is given in Table 5. The hyperparameters used in the proposed model were determined using the trial and error method in the experimental process. In training the model; minimum learning rate = 1e−06, optimization = adam, loss = categorical cross-entropy, metrics = ['accuracy', 'precision', 'recall'], batch size = 32, number of epochs = 50, patience = 2, factor = 0.5, mode = min, save best only = true were used (Table 7).

$$\texttt{new\_lr} = \texttt{lr*factor} \quad (14)$$

lr: learning rate, factor: learning rate reduction coefficient.

Table 5
Pseudocode for COVID-DSNet training and test.

Algorithm Training and test procedure for COVID-DSNet
Input: CT, CXR ve CT + CXR images training, validation, and test images divided; labelled; K: epoch.
Output: trained model m; normal, bacterial pneumonia, viral pneumonia and Covid-19 classification, statistical analysis
1: (X) ← (pre-processing (resize [CT, CXR, and CT + CXR images in 224 x 224 x 3 dimesion], 0-1 normalization) data)
2: (Y) ← (class label [normal, bacterial pneumonia, viral pneumonia, and covid-19])
3: (train_x, train_y), (test_x, test_y) ← split ((X, Y), split size = 0.3)
4: (val_x, val_y) ← validaiton split ((train_x, train_y), split size = 0.1)
5: **for** i = 1 to K, **do**
6: m(t) ← model_train (adam, categorical crossentropy (train_x, train_y))
7: m(e) ← model_evaluate (m(t), (val_x, val_y))
8: **end for**
9: mbest ← save best_model{(m(t), m(e)), Iteration = 1, 2, …, K}
10: pred ← model_predict (mbest, (test_x))
11: evaluation results ← statistical analysis (test_y, pred)

3.4. The performance audit of COVID-DSNet architecture

Datasets consisting of COVID-DSNet architecture CT, CXR, and CT + CXR medical images were used to classify normal, bacterial pneumonia cases, viral pneumonia cases, and Covid-19 cases considering the dual, triple and quadruple class categories. The model was trained and tested with the classification studies' training and validation test approach. In addition, the K-fold cross-validation method was applied for the performance analysis of the COVID-DSNet architecture. Accuracy, positive predictive value, sensitivity, f1-score, cohen's kappa, confusion metrics, training loss/accuracy, validation loss/accuracy graphics were used to evaluate the experimental results of the COVID-DSNet architecture. The results of the empirical studies with the COVID-DSNet architecture are given in Section 5.

4. Materials and methods

InceptionResNetV2, InceptionV3, MobileNet, ResNet-101, DenseNet-169, NASNetMobile, EfficientNetB0 algorithms from modern deep neural networks are used together with the proposed COVID-DSNet architecture for the detection of normal, bacterial pneumonia, viral pneumonia, and Covid-19 from CT, chest X-ray images. Accuracy, Positive Predictive Value, Sensitivity, F1-score, and Cohen's Kappa metrics were used to evaluate the experimental results.

In this section, the dataset consisting of CT, CXR, hybrid CT + CXR images is in Section 4.1, the theoretical infrastructure of modern deep neural networks applied for the classification of Covid-19 infection is in Section 4.2, the hyperparameters used in current architectures with the proposed architecture are in Section 4.3. Furthermore, the theoretical background of the K-fold cross-validation method applied in the performance evaluation of the proposed architecture is given in Section 4.4. Finally, the mathematical expressions of the performance metrics used in evaluating binary and multi-class classification results are provided in Section 4.5.

4.1. Dataset description

This study used datasets consisting of CT, chest X-ray, and CT + chest X-ray images. Within the scope of the study 2357 data were used in the CT dataset 2515 data in the chest X-ray dataset and 2400 data in the hybrid CT + chest X-ray dataset. In addition, 70 % of the dataset samples (training + validation) consisting of CT, chest X-ray, and CT + chest X-ray images were used in the training of the models, and 30 % of the remaining data were used in the testing process of the models (Table 6). Sample data of CT, chest X-ray, and CT + chest X-ray images are given in Fig. 7. The CT dataset used in the study consists of the "COVID-19 and common pneumonia chest CT dataset [86]" and the "a COVID-19 multiclass dataset of CT scans". The CT dataset consists of the triple

categories of Non-COVID-19, Common pneumonia, and COVID-19. Images were selected randomly as 757-non-COVID-19 images, 800- common pneumonia images, and 800-COVID-19 images from the data files. In the classification studies made with the CT dataset, 1649 CT data were used to train deep neural networks (train + validation), and 708 test data were used to test the networks. Chest X-ray medical images, another dataset used in the study, were compiled from two separate sources: (a) COVID-19 Radiography Database prepared by Rahman et al. [87] and (b) Chest X-Ray Images (Pneumonia) prepared by Kermany et al. [88]. The chest X-ray dataset, compiled with the "COVID-19 Radiography Database" and "Chest X-Ray Images (Pneumonia)" datasets, consists of four categories: normal, bacterial pneumonia, viral pneumonia, COVID-19. In the study, 700 normal, 515 bacterial pneumonia, 600 viral pneumonia, and 700 COVID-19 data were randomly selected from the "COVID-19 Radiography Database" and "Chest X-Ray Images (Pneumonia)" datasets were used. In the classification studies made with the CXR dataset, 1760 CXR data were used in training (train + validation) of deep neural networks and 755 test data to test the networks. Finally, the hybrid CT + CXR cluster created with the "COVID-19 and common pneumonia chest CT dataset", "a COVID multiclass dataset of CT-scans"and "COVID-19 Radiography Database" datasets were used within the scope of the study. The dataset consists of two categories, Non-COVID-19 and COVID-19. Hybrid CT with 600 Normal, 600 COVID-19 data samples randomly selected from the "COVID-19 and common pneumonia chest CT dataset" and "a COVID multiclass dataset of CT-scans" datasets 600 Non-COVID-19, 600 COVID-19, and "COVID-19 Radiography Database" randomly selected dataset + The CXR dataset was created. In the classification studies with the CT + CXR dataset, 1680 CXR data were used in training (train + validation) of deep neural networks, and 720 test data were used to test the networks.

Table 6
Dataset details.

Medical imaging technique	Dataset	Categories	Data	Train + validation/ test	Link
CT	A COVID multiclass dataset of CT scans + COVID-19 and common pneumonia chest CT dataset	Non-COVID-19 Common pneumonia COVID-19	757 800 800	1649/708	https://doi.org/10.17632/3y55vgckg6.2 https://doi.org/10.17632/ygvgkdbmvt.1 https://doi.org/10.34740/kaggle/dsv/1235046 (Accessed 14 January 2022)
Chest X-Ray	COVID-19 Radiography Database + Chest X-Ray Images (Pneumonia)	Normal Bacterial pneumonia Viral pneumonia COVID-19	700 515 600 700	1760/755	https://www.kaggle.com/datasets/tawsifurrahman/covid19-radiography-database https://doi.org/10.17632/rscbjbr9sj.2 (Accessed 14 January 2022)
CT + Chest X-Ray	A COVID multiclass dataset of CT scans + COVID-19 and common pneumonia chest CT dataset + COVID-19 Radiography Database	Non-COVID-19 COVID-19	1200 1200	1680/720	https://doi.org/10.17632/3y55vgckg6.2 https://doi.org/10.17632/ygvgkdbmvt.1 https://doi.org/10.34740/kaggle/dsv/1235046 https://www.kaggle.com/datasets/tawsifurrahman/covid19-radiography-database (Accessed 14 January 2022)

4.2. Deep learning algorithm

In addition to the proposed COVID-DSNet architecture for the detection of normal, bacterial pneumonia, viral pneumonia and Covid-19 in datasets consisting of CT, chest X-ray and CT + chest X-ray medical images, ResNet-101 [82], DenseNet from deep convolutional neural networks −169 [83], InceptionResNetV2 [89], InceptionV3 [90], MobileNet [91], NASNetMobile [92], EfficientNetB0 [93] architectures are also used. In this section, the theoretical framework of the algorithms is given. The flow chart of InceptionV3, ResNet-101, DenseNet-169, and MobileNet architectures is given in Fig. 8.

a) ResNet-101: He et al. it is a deep convolutional neural network architecture proposed. He et al. to solve the gradient disappearance problem in deep neural networks, proposed residual networks that form the basis of the ResNet architecture. ResNet architecture has different versions according to the number of layers 50, 101, 152. In this study, 101-layer ResNet-101 architecture was used. The ResNet-101 architecture consists of 224 × 224 input sizes, 101 layers, and approximately 45 million parameters. The network trained with the ImageNet dataset produced a successful performance.

b) DenseNet-169: Huang et al. It is a deep convolutional neural network architecture proposed in 2017. Huang et al. proposed a method that increases the reuse of features to solve the gradient disappearance problem in deep neural networks. The proposed method directly connects the layers using the feed-forward method. Each layer is directly connected to all previous layers in architecture, thus providing direct access to feature vectors generated from previous layers. Accessed attributes are used as input by combining them with the concatenate layer in a certain layer. DenseNet-169 architecture is backbone of DenseNet blocks (DenseBlock). The DenseNet-169 architecture consists of 224 × 224 input size, 169 layers, three transition layers, four dense blocks, a softmax output layer, and approximately 14.3 million parameters. The architecture trained with the ImageNet dataset produced a successful performance in the ILSRVRC ImageNet image processing competition.

c) InceptionResNetV2: Szegedy et al. is a deep convolutional neural network architecture proposed in 2016. InceptionResNetV2 architecture was developed with a hybrid approach inspired by Inception and ResNet architecture. ResNet networks are used to solve the gradient disappearance problem in the network. The InceptionResNetV2 architecture consists of 299 × 299 input sizes, 164 layers, and approximately 56 million parameters. The network trained with the ImageNet dataset produced a successful performance.

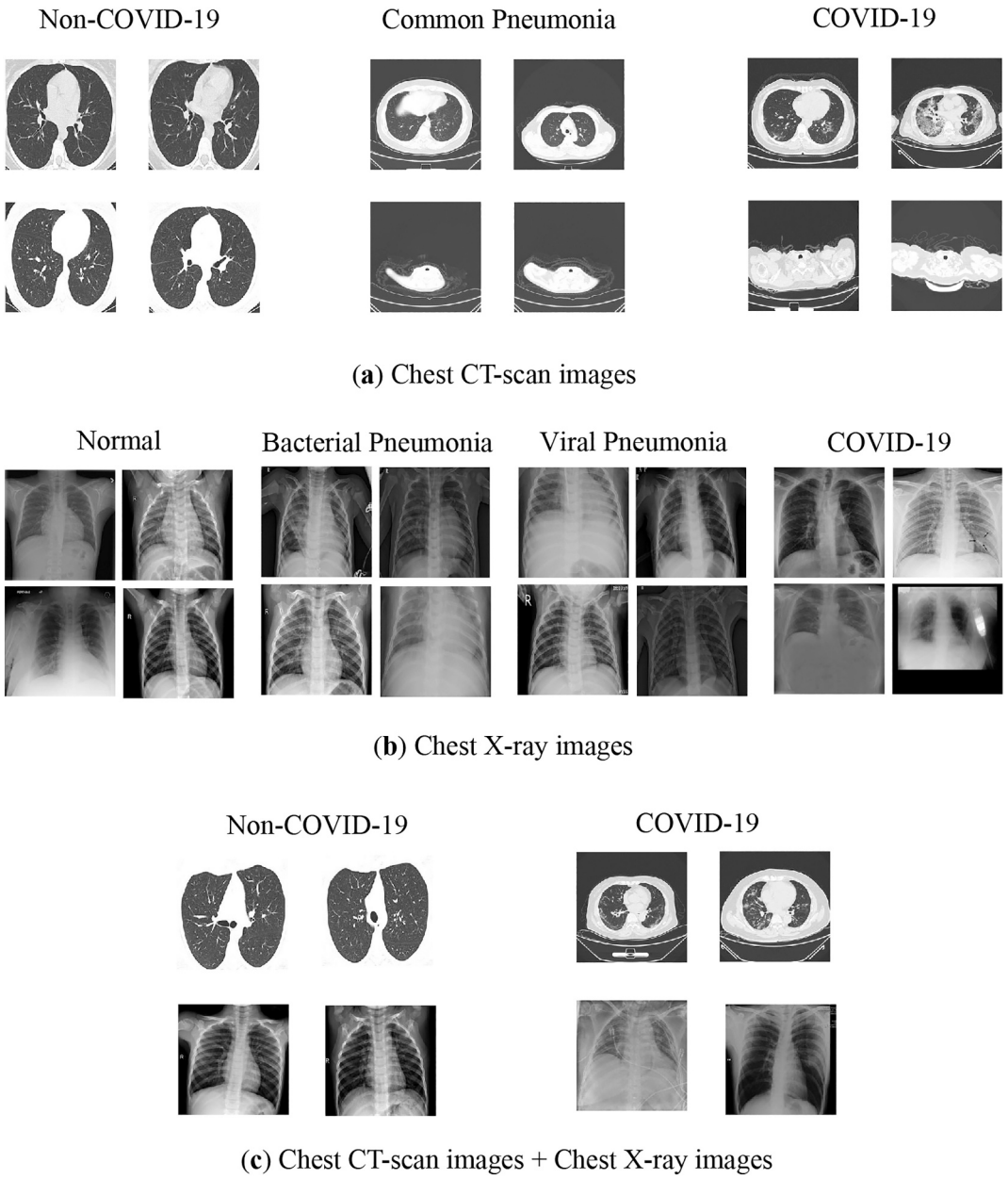

Fig. 7. Sample images from the dataset a. Chest CT-scan images: Non-COVID-19, Common Pneumonia, and COVID-19. b. Chest X-Ray images: Normal, Pneumonia with Viral infection and Pneumonia with Bacterial infection and COVID-19. c. Hybrid Chest CT-scan images + Chest X-Ray images: Non-COVID-19 and COVID-19.

d) InceptionV3: The GoogLeNet architecture that Szegedy et al. introduced at the 2014 ILSRVRC ImageNet image processing competition. The GoogLeNet architecture InceptionV3 was the most successful model with the lowest error value in the competition. Additional feature vectors are used to solve the gradient disappearance problem in InceptionV3 architecture. The InceptionV3 architecture consists of 299 × 299 input sizes, 154 layers, and approximately 24 million parameters. GoogLeNet architecture has been developed within the framework of the Inception module, which consists of 5 × 5, 3 × 3, 1 × 1 convolution, 3 × 3 max pooling, and concatenate layers. The InceptionV3 architecture is different from the GoogLeNet Inception module.

1. In Inception module A, the 5 × 5 convolution layer in the Inception module is divided into two 3 × 3 convolution layers;
2. In Inception module B, the 3 × 3 and 5 × 5 convolution layers in the Inception module are divided into symmetrical 7 × 7 convolution layers, and the separated 7 × 7 symmetrical convolution layers are divided into asymmetric 1 × 7, and 7 × 1 convolution layers;
3. In Inception module C, the 3 × 3 symmetric convolution layer in the Inception module is divided into asymmetric 1 × 3, and 3 × 1 convolution layers, the 5 × 5 convolution layer in the Inception module is divided into a 3 × 3 convolution layer, and separated symmetric convolution layer is converted into asymmetric 1 × 3, and 3 × 1 convolution layers;
4. Max pooling, asymmetric convolution network, and parallel symmetric convolution network are implemented in the reduction module.

e) MobileNet: It is a lightweight deep convolutional neural network architecture proposed by Howard et al. The depthwise separable convolution layer, which is an advantageous method by reducing the number of parameters in the architecture and calculation volume, constitutes the basic building block of the MobileNet architecture. 3 × 3

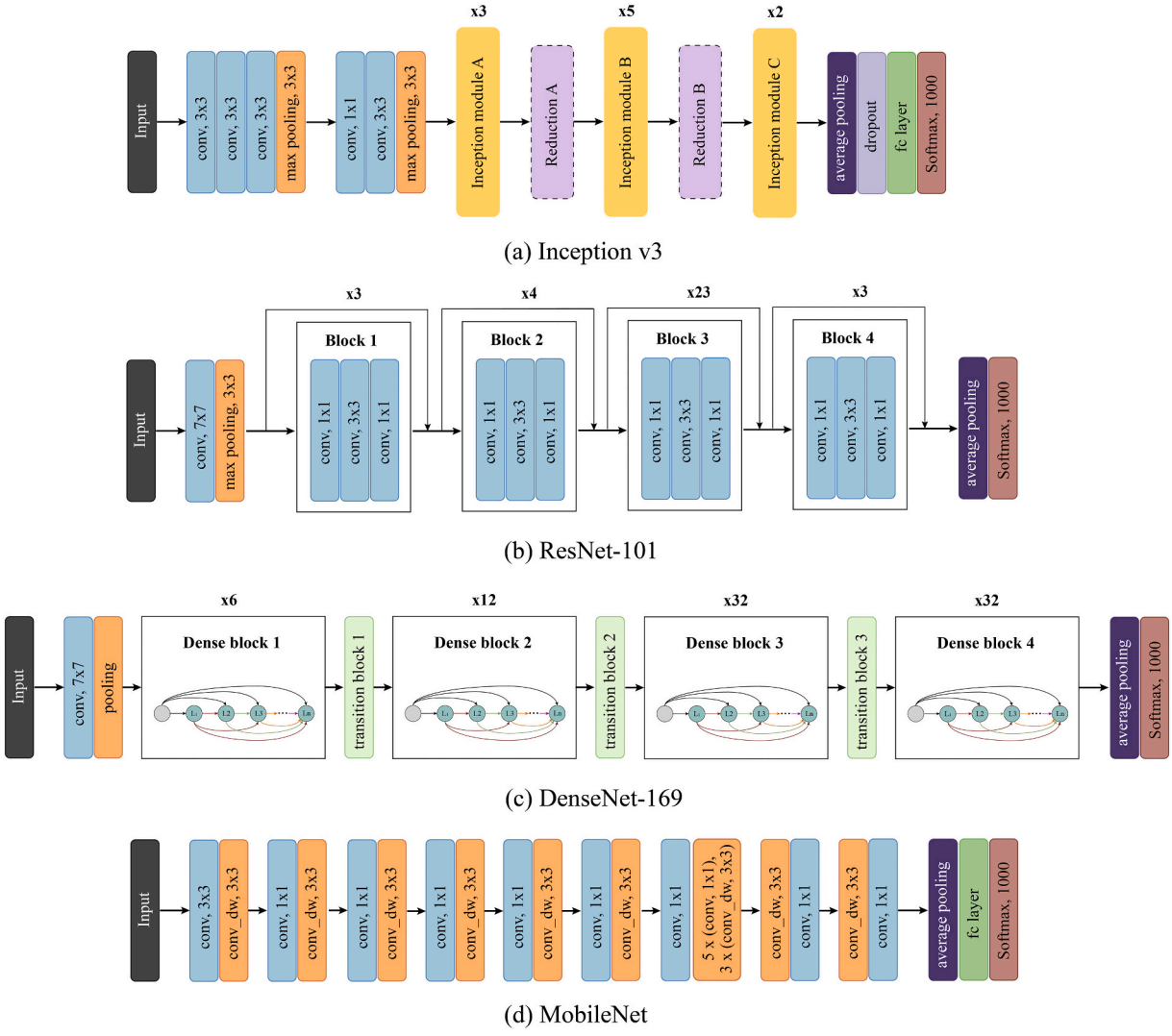

Fig. 8. Architectures of the four CNN base classifiers: (a) Inception v3, (b) ResNet-101, (c) DenseNet-169, and (d) MobileNet.

depth-wise convolution and 1 × 1 point-wise convolution layers were used in the architecture. The MobileNet architecture consists of 224 × 224 input sizes, 28 layers, and 4.3 million parameters. The network trained with the ImageNet dataset produced a successful performance.

f) NASNetMobile: The architecture proposed by Zoph et al. is a deep convolutional neural network architecture consisting of convolutional cells, normal cells, and reduction cells. The NASNet architecture was not developed directly by the developers. Instead, the architecture was produced due to the Neural Architecture Search method used to discover neural networks. The Neural Architecture Search architecture uses reinforcement learning for the best values of hyperparameters, layer type, and the number of layers. The NASNet architecture was found, with the Neural Architecture Search method implemented in the CIFAR-10 dataset. The resulting architecture was also applied to the ImageNet dataset, and new architecture was obtained. NASNetMobile architecture consists of 224 × 224 input size, and 5.3 million parameters. The network trained with the ImageNet dataset produced a successful performance.

g) EfficientNetB0: Tan et al. is the proposed deep convolutional neural network architecture. The architecture uses the inverted bottleneck residual blocks and squeeze-and-excitation blocks structure in the MobileNetV2 architecture. In addition, the Swish activation function, which is the product of linear and sigmoid activation, was proposed by the authors within the scope of familiarization. The EfficientNetB0 architecture consists of 224 × 224 input sizes, and 5.3 million parameters. The network trained with the ImageNet dataset produced a successful performance.

4.3. Hyperparameters used in deep learning algorithms

In this section, the theoretical infrastructure of the proposed COVID-DSNet, COVID-DSNet + FCC, COVID-DSNet + LSTM architectures and hyperparameters used in deep convolutional neural networks InceptionResNetV2, InceptionV3, MobileNet, ResNet-101, DenseNet-169, NASNetMobile, EfficientNetB0 algorithms are given. Hyperparameters are given in Table 7. All deep neural networks used in the study were trained and tested under the same conditions. All models were trained with training and validation testing for 50 iterations. During the training of the models, man optimization algorithm, learning rate and 'accuracy,' 'precision,' and 'recall' metrics were used. During the training, the learning rate value is decreased when the learning decreases and the validation loss increases. Within the scope of the study, if the validation loss value did not decrease during two cycles according to the patience parameter, the learning rate value was reduced by 0.5 compared to the factor parameter. The loss function used is categorical cross-entropy. During the training of the models, weight vectors were obtained throughout the cycle. Only the weight vector/network with the lowest validation loss value was recorded, considering the Monitor and Save

Table 7
Hyperparameters.

Hyper parameters	Value
Input shape	224 × 224 × 3
Epoch	50
Batch size	32
Patience	2
Factor	0.5
Metrics	'accuracy', 'precision', 'recall'
Loss	'categorical_crossentropy'
Optimizer	'adam'
Monitor	'val_loss'
Save best only	true
Mode	'min'
Initial learn rate	1e-06

Best Only parameters. The weight vector with the lowest loss value was evaluated empirically with the test dataset.

Input Shape; Input layer size of deep neural networks. With the proposed model, the input size of the deep neural networks used in the study was determined as 224 × 224 × 3.

Epoch; the number of cycles in training the model. Batch size; It is the number of sub-samples that can be used simultaneously in the forward and backward propagation of the networks in the training phase. Batch size value may vary according to ram capacity. A batch size of 32 is used in all algorithms. Patience; the number of cycles where the training stops, the loss value does not decrease (epoch). After the Patience value, the learning rate will decrease. The value of patience was determined as 2 in the study. Factor; the amount by which the learning rate will decrease. In the study, the factor value was determined as 0.5. Metrics; List of metrics to be evaluated by models during training and testing phases.

Accuracy, precision, and recall metrics were used in the study. Monitor_SaveBestOnly_Mode; deep learning architectures produce weight vectors as many as the number of epochs. This study recorded the architecture with the lowest validation loss (monitor: 'val_loss'). The network with the lowest error value (mode: 'min') was evaluated empirically with the test dataset. Learning rate; is the rate of convergence of backpropagation. It determines the rate of change of step size in updating the weights (according to the loss gradient) during the training of the model.

The minimum learning rate value in the study was determined as 1e-06. Loss Function; the function to be maximized or minimized is called the objective function. When the value of the objective function is minimized, it is called the cost, error or loss function. One of the critical steps in the training of deep neural networks is to minimize or reset the error values.

In this study, categorical cross-entropy, which is used in multiple classification studies, was used.

The mathematical output of the categorical cross-entropy function is as follows.

$$L_{CCE}\ (y, \hat{y}) = -\frac{1}{N}\sum_{i=0}^{m}\sum_{j=0}^{n}\left(y_{ij} * log\left(\hat{y}_{ij}\right)\right) \tag{15}$$

where; y represents the actual and, ŷ the predicted values.

Optimizer; in this study, the use of man (Adaptive Momentum) was suggested by Kingma et al. [94]. It is a Gradient design used for visiting entropy inspection related to man descent optimization. The Adam optimization function can generate a hybrid population using the Adagrad and momentum methods. When the root learning problem arises due to the use of the Adagrad function, the Mean Square Propagation (RMSprop) method was used whether the man is the output of the function.

$$g_t = \nabla_\Theta f_t\ (\Theta_{t-1}) \tag{16}$$

$$m_t = \beta_1 m_{t-1} + (1-\beta_1) g_t \tag{17}$$

$$v_t = \beta_2 v_{t-1} + (1-\beta_2) g_t^2 \tag{18}$$

$$m_t^{'} = \frac{m_t}{1-\beta_1^t} \tag{19}$$

$$v_t^{'} = \frac{v_t}{1-\beta_2^t} \tag{20}$$

$$\Theta_{t+1} = \Theta_t - \frac{\alpha}{\sqrt{v_t^{'}} + \varepsilon}\, m_t^{'} \tag{21}$$

where; Variable $\beta_1 ve\ \beta_2$ are hyperparameters, variables ε ve α are learning coefficient, g calculated gradient, m_t is the exponential mean of the gradient, Θ updated value, v_t is the exponential mean of the squares of the gradient, and $\nabla_\Theta f_t\ (\Theta_{t-1})$ indicates the gradient of the cost function.

4.4. Cross-validation

Cross-validation is a model validation technique that helps a model reveal its accuracy and classification success on an independent dataset. Cross-validation is a critical method in developing a model to identify over-learning (overfitting the model to the dataset) and under-learning. It is discovering the best model aimed with the cross-validation method. In this method, the original data is divided into k parts; while the k-1 number of factors is used to train the model, the remaining amount is used to test the model's accuracy (validation set or test set). The process here repeats every k count. In this study, a five k-fold cross-validation method was applied. The flow chart of the used method is given in Fig. 9.

According to Fig. 9, the original data is divided into train and test datasets. The Train dataset is divided into five parts. While four pieces were used for the train set, one piece was used to validate the model. At the end of each fold, weight vectors were recorded according to the lowest validation loss value and tested (with test dataset).

4.5. Evaluation metrics

The classification success of a model is determined by comparing the number of samples assigned to the correct class with the number of samples assigned to the wrong class. Accuracy, Positive Prediction Value, Sensitivity, F1-score, and Cohen's Kappa performance criteria were used to evaluate the success of the proposed architectures and deep neural networks models InceptionResNetV2, InceptionV3, MobileNet, ResNet-101, DenseNet-169, NASNetMobile, EfficientNetB0. In the study, binary and multiclass classification was made. This section gives mathematical equivalents of performance criteria and complexity matrix details of binary and multiclass methods.

4.5.1. Performance metrics for binary classification

The confusion matrix consists of a 2 × 2 dimensional matrix in binary classification studies. In the problem of diagnosis of COVID-19, if one of the labels is considered COVID-19 and the other to Non-COVID-19, matrix elements are determined by comparing the actual class label (COVID-19, Non-COVID-19) and the predicted class label (COVID-19, Non-COVID-19). The complexity matrix of binary classification problems is given in Table 8. The columns in the matrix in Table 8 show examples of predicted classes, while the rows show examples of actual classes. According to Table 8, for example; In the study of diagnosis of patients with COVID-19 infection; TP: It is determined that the patient who is actually COVID-19 is also COVID-19 as a result of the estimation study, TN: The actual Non-COVID-19 prediction result is also Non-COVID-19, FP: Actually Non-COVID-19 but the prediction result is COVID-19 -19, FN: It is actually COVID-19, but the forecast result is Non-COVID-19.

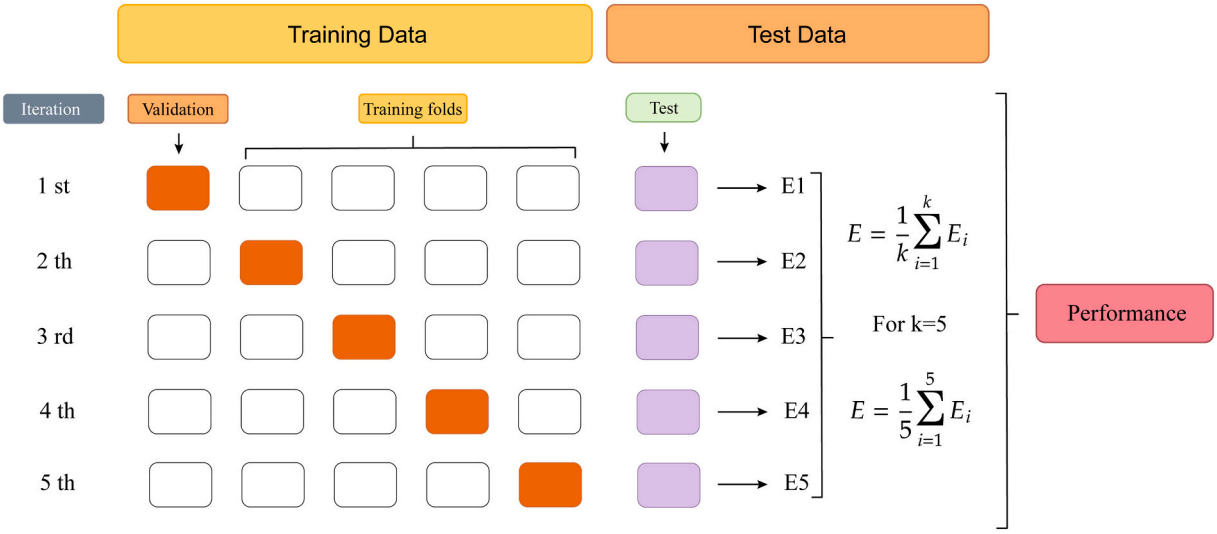

Fig. 9. 5 cross-validation and test diagram.

Table 8
Binary classification confusion matrix.

		Predicted class	
		Negative (**N**)	Positive (**P**)
Actual class	Negative (**N**)	True negative (**TN**)	False positive (**FP**)
	Positive (**P**)	False negative (**FN**)	True positive (**TP**)

According to Table 9, ACC: ratio of correctly predicted samples to all samples; PPV: number of positive samples predicting correctly, the proportion of models predicting positive, SN: ratio of positive samples predicting correctly to the number of samples predicting all positive and negative, F1: a proposed hybrid performance measure combining the PPV and TPR success measures. The mathematical expressions of the ACC, PPV, SN, F1, and κ metrics are given in Table 9.

4.5.2. Performance metrics for multi-class classification

In multidimensional classification studies, the confusion matrix consists of an n × n dimensional matrix. The complexity matrix of 3-class classification problems is given in Table 10. In case X class is selected as TP according to Table 10; It is calculated as FP = YX + ZX, FN = XY + XZ, TN = YY + ZZ. If Y class is selected as TP, it is calculated as FP = XY + ZY, FN = YX + YZ, TN = XX + ZZ. If Z class is selected as TP, it is calculated as FP = XZ + YZ, FN = ZX + ZY, TN = XX + YY. In Table 10, TP values show correctly predicted class values, while E shows incorrectly predicted class values.

In multi-class classification studies, PPV, SN, and F1 metrics are calculated according to each metric's average (micro, macro, weighted)

Table 9
The performance metrics of the binary classification.

Metric	Formula
Accuracy	$ACC = \frac{TP + TN}{TP + TN + FP + FN}$
Positive Predictive Value (Precision)	$PPV = \frac{TP}{TP + FP}$
Sensitivity (Recall)	$SN = \frac{TP}{TP + FN}$
F_1-Score	$F_1 = 2 \times \frac{PPV \times TPR}{PPV + TPR}$
Cohen's Kappa	$Kappa = \kappa = \frac{p_o - p_e}{1 - p_e}; p_o = ACC$ $p_e = \frac{\sum_{c=1}^{N}(TP_c + FP_c) \times (TP_c + FN_c)}{(TP + TN + FP + FN)^2}$

Table 10
Multi-class classification confusion matrix (when Y class is selected as TP).

		Predicted class		
		Class X	Class Y	Class Z
Actual class	Class X	TP (XX)	E (XY) FP	E (XZ)
	Class Y	E (YX) FN	TP (YY)	E (YZ) FN
	Class Z	E (ZX)	E (ZY) FP	TP (ZZ)

parameter, unlike binary classification. Micro, macro, weighted values of PPV, SN, F1 metrics are calculated according to the equations in Table 11.

5. Experimental results

In this section, COVID-DSNet, COVID-DSNet + FCC, COVID-DSNet + LSTM, which are recommended for the diagnosis of normal, bacterial pneumonia, viral pneumonia, COVID-19 diseases in CT, CXR and hybrid CT + CXR medical images, are modern architectures InceptionResNetV2, InceptionV3, MobileNet, Empirical results of ResNet-101, DenseNet-169, NASNetMobile, EfficientNetB0 algorithms are given. All architectures are trained with train dataset and validation dataset under the same conditions, then tested (with test set). In the study, medical images in the CT dataset (Non-COVID-19, Common Pneumonia, COVID-19) and chest X-ray dataset (Normal, Bacterial Pneumonia, Viral Pneumonia, COVID-19) and binary and multi-class classification, hybrid CT + Binary classification was made with CXR (Non-COVID-19, COVID-19) medical images and experimental results are given in this section. In addition, the experimental results of the K-fold cross-validation method applied for the performance analysis of the COVID-DSNet architecture are given. Within the scope of the study, accuracy, PPV, SN, F1, Kappa performance criteria, confusion metrics, training loss/accuracy, and validation loss/accuracy graphs were used to evaluate the experimental results.

5.1. Performance results on chest CT image dataset

Multi-class (triple) and binary (binary) classification was made with the CT dataset consisting of three categories: Non-COVID-19, Common Pneumonia, COVID-19. In the multi-class classification problem, the proposed COVID-DSNet, COVID-DSNet + FCC, COVID-DSNet + LSTM

Table 11
The performance metrics of the multi-class classification.

Metric	Formula
Positive Predictive Value (Precision)	$PPV\ (YY) = \frac{TP\ (YY)}{TP\ (YY) + E\ (XY) + E\ (ZY)}$
Sensitivity (Recall)	$SN\ (YY) = \frac{TP\ (YY)}{TP\ (YY) + E\ (YX) + E\ (YZ)}$
F_1-Score	$F_1 = 2 \times \frac{PPV\ (YY) \times SN\ (YY)}{PPV\ (YY) + SN\ (YY)}$
Positive Predictive Value (macro average)	$PPV\ (macro) = \frac{1}{N}\sum_{c=1}^{N} PPV\ (c)$
Sensitivity (macro average)	$SN\ (macro) = \frac{1}{N}\sum_{c=1}^{N} SN\ (c)$
F_1-Score (macro average)	$F_1\ (macro) = \frac{1}{N}\sum_{c=1}^{N} F_1\ (c)$
Positive Predictive Value (micro average)	$PPV\ (micro) = \frac{\sum_{c=1}^{N} TP\ (c)}{\sum_{c=1}^{N} [TP\ (c) + FP\ (c)]}$
Sensitivity (micro average)	$SN\ (micro) = \frac{\sum_{c=1}^{N} TP\ (c)}{\sum_{c=1}^{N} [TP\ (c) + FN\ (c)]}$
F_1-Score (micro average)	$F_1\ (micro) = 2 \times \frac{PPV\ (micro) \times SN\ (micro)}{PPV\ (micro) + SN\ (micro)}$
Positive Predictive Value (weighted average)	$PPV\ (weighted) = \frac{\sum_{c=1}^{N} (PPV\ (c) \times \text{all instances in class c})}{\text{all instances}}$
Sensitivity (weighted average)	$SN\ (weighted) = \frac{\sum_{c=1}^{N} (SN\ (c) \times \text{all instances in class c})}{\text{all instances}}$
F_1-Score (weighted average)	$F_1\ (weighted) = \frac{\sum_{c=1}^{N} (F_1\ (c) \times \text{all instances in class c})}{\text{all instances}}$

architectures and deep convolutional neural networks InceptionResNetV2, InceptionV3, MobileNet, ResNet-101, DenseNet-169, NASNetMobile, EfficientNetB0 algorithms were applied. The proposed COVID-DSNet architecture in the binary classification problem has been applied. In the multi-class and binary classification problem, 70 % of the dataset consisting of CT medical images is divided into training (10 % of the training dataset was used for the validation dataset) and 30 % as the test dataset. In the multi-class classification problem, While 1649 data were used in the training of the models, 708 data were used in the testing process of the models. According to the experimental results, COVID-DSNet was the most successful model in the multi-class classification problem with the CT dataset. In the multi-class classification problem; While the COVID-DSNet architecture predicts with 97.60 % accuracy; InceptionResNetV2, InceptionV3, MobileNet, ResNet-101, DenseNet-169, NASNetMobile, EfficientNetB0, COVID-DSNet + LSTM, and COVID-DSNet + FCC networks 93.22 %, 95.62 %, 93.50 %, 94.49 %, 96.05 %, 63.28 %, respectively, It estimated 89.41 %, 96.33 %, and 96.19 % accuracy (Table 12). COVID-DSNet architecture While 100 %, 96.69 %, and 96.17 % experimental results were obtained in the diagnosis of Non-COVID-19, Common Pneumonia, COVID-19, respectively, according to the PPV success criteria; In the CT dataset multi-class problem, the second-best architecture DenseNet-169 architecture was 100 %, 92.83 %, and 95.58 % experimental results were obtained in the diagnosis of Non-COVID-19, Common Pneumonia, COVID-19, respectively, according to the PPV performance criterion. The trainable parameters of COVID-DSNet, DenseNet-169, and MobileNet architectures are 4.17 M (million), 12.49 M, and 3.21 M, respectively.

In multi-class classification studies, PPV, SN, and F1 performance criteria are calculated according to micro avg., macro avg., and weighted avg. values. Within the scope of the study, COVID-DSNet, COVID-DSNet + FCC, COVID-DSNet + LSTM, InceptionResNetV2, InceptionV3, MobileNet, ResNet-101, DenseNet-169, NASNetMobile, and EfficientNetB0 applied in the detection of Non-COVID-19, Common Pneumonia, COVID-19 The PPV, SN, and F1 performance criteria of the networks were calculated according to micro, macro and weighted values and the analysis results are given in Table 13. PPV_{micro}, PPV_{macro}, and $PPV_{weighted}$ metric results of the COVID-DSNet architecture were 97.60 %, 97.62 %, 97.60 %, respectively; DenseNet-169 architecture's PPV_{micro}, PPV_{macro}, and $PPV_{weighted}$ measured results were 96.04 %, 96.13 %, 96.08 %, respectively; MobileNet architecture's PPV_{micro},

Table 12
Performance of all deep neural network architectures on COVID-19 and common pneumonia chest CT test dataset (with train-validation-test split approach). CP: Common Pneumonia, Params (M), ACC (%), Kappa (%), PPV (%), SN (%), F_1 (%).

Network	Params	Class	ACC	Kappa	PPV	SN	F_1
InceptionResNetV2	54.28	Non-COVID-19	93.22	89.84	100	100	100
		CP			96.21	83.54	89.43
		COVID-19			84.96	96.58	90.40
InceptionV3	21.77	Non-COVID-19	95.62	93.43	100	100	100
		CP			91.41	96.30	93.79
		COVID-19			95.93	90.60	93.19
MobileNet	3.21	Non-COVID-19	93.50	90.25	100	100	100
		CP			88.33	93.42	90.80
		COVID-19			92.73	87.18	89.87
ResNet-101	42.56	Non-COVID-19	94.49	91.74	100	100	100
		CP			92.50	91.36	91.93
		COVID-19			91.14	92.31	91.72
DenseNet-169	12.49	Non-COVID-19	96.05	94.07	100	100	100
		CP			92.83	95.88	94.33
		COVID-19			95.58	92.31	93.91
NASNetMobile	4.24	Non-COVID-19	63.28	44.62	86.54	97.40	91.65
		CP			50.45	91.77	65.11
		COVID-19			0	0	0
EfficientNetB0	4.01	Non-COVID-19	89.41	84.13	100	100	100
		CP			92.86	74.90	82.92
		COVID-19			78.29	94.02	85.44
COVID-DSNet + LSTM	7.34	Non-COVID-19	96.33	94.49	100	100	100
		CP			95.02	94.24	94.63
		COVID-19			94.07	94.87	94.47
COVID-DSNet + FCC	4.25	Non-COVID-19	96.19	94.28	100	100	100
		CP			96.15	92.59	94.34
		COVID-19			92.59	96.15	94.34
COVID-DSNet	4.17	Non-COVID-19	97.60	96.40	100	100	100
		CP			96.69	96.30	96.49
		COVID-19			96.17	96.58	96.38

Table 13
Empirical results of $PPV_{micro,\ macro,\ weighted}$ (%), $SN_{micro,\ macro,\ weighted}$ (%), and $F1_{micro,\ macro,\ weighted}$ (%) performance metrics of deep learning Algorithms (with train-validation-test split approach). Avg 1: Micro, Avg 2: Macro, Avg 3: Weighted.

Network	PPV			SN			F_1		
	Avg1	Avg2	Avg3	Avg1	Avg2	Avg3	Avg1	Avg2	Avg3
InceptionResNetV2	93.22	93.72	93.73	93.22	93.37	93.22	93.22	93.28	93.20
InceptionV3	95.62	95.78	95.70	95.62	95.63	95.62	95.62	95.66	95.62
MobileNet	93.50	93.68	93.59	93.50	93.53	93.50	93.50	93.56	93.49
ResNet-101	94.49	94.55	94.50	94.49	94.55	94.49	94.49	94.55	94.49
DenseNet-169	96.04	96.13	96.08	96.04	96.06	96.05	96.04	96.08	96.04
NASNetMobile	63.28	45.66	45.55	63.28	63.06	63.28	63.28	52.25	52.25
EfficientNetB0	89.41	90.38	90.37	89.41	89.64	89.41	89.41	89.45	89.32
COVID-DSNet + LSTM	96.33	96.36	96.33	96.33	96.37	96.33	96.33	96.36	96.33
COVID-DSNet + FCC	96.19	96.25	96.23	96.19	96.25	96.19	96.19	96.23	96.19
COVID-DSNet	97.60	97.62	97.60	97.60	97.63	97.60	97.60	97.62	97.60

PPV_{macro}, and $PPV_{weighted}$ metric results are 93.50 %, 93.68 %, 93.59 %, respectively.

The confusion matrix of COVID-DSNet and DenseNet-169 networks is given in Fig. 10. In Fig. 11, loss, accuracy, PPV, and SN graphs of deep neural networks trained on the CT dataset. In Fig. 12, validation loss, validation accuracy, validation PPV, and validation SN graphs of the validation dataset used in testing deep neural networks during training are given.

According to Fig. 10, in the multi-class study with the chest CT dataset, the COVID-DSNet architecture, the most successful model, misdiagnosed 17 medical images from 708 test data. In contrast, the second-best architecture, DenseNet169 architecture, misdiagnosed 28 medical images from 708 test data.

5.1.1. COVID-19 detection with COVID-DSNet and improved COVID-DSNet models

COVID-DSNet architecture is a deep convolutional neural network architecture developed with add layer, concatenate, Conv2D 1-2-3-4, transition layer components providing additional feature vectors. This section discusses the effects of additional feature vectors of the structures that make up the architecture. Experimental results are given in Table 14. In addition, the column chart of the experimental results is shown in Fig. 13.

According to the experimental results in Table 14, the COVID-DSNet architecture produced a prediction with 97.60 % accuracy with all its components. Furthermore, of the components in the COVID-DSNet architecture, 96.75 % accuracy was obtained when only the add layer was not used, and 93.79 % accuracy was obtained when only the conv1-2-3-4 layer was not used. As a result, it has been observed that each component that makes up the architecture improves the architecture's performance in detecting infection.

5.1.2. Binary and multi-class classification with COVID-DSNet architecture

The CT dataset consists of three categories: Non-COVID-19, Common Pneumonia, COVID-19. The categories in the dataset were arranged as non-covid19/covid-19, common pneumonia/covid-19, all others/covid-19 so that the dataset consisting of CT images can be applied to the binary classification study. The COVID-DSNet architecture was used in the classification of the two-class categories. The COVID-DSNet architecture showed 97.60 % classification success in the triple (non-covid19/common pneumonia/covid-19) classification study. The binary classification study conducted with the COVID-DSNet architecture using the non-covid19/covid-19 categories correctly predicted the samples with both categories in the test dataset. It showed a classification success with 100 % accuracy (Table 15). The complex matrix of the binary and triple classification study with the COVID-DSNet architecture is given in Fig. 14.

According to Fig. 14, the triple (non-covid19/common pneumonia/covid-19) classification study with the COVID-DSNet architecture misdiagnosed 17 medical images out of 708 test data. In contrast, the binary with the architecture non-covid19/covid-19 correctly diagnosed all 468 test data in the classification study, misdiagnosed 34 medical images out of 480 test data in the dual classification study with common pneumonia/covid-19. Finally, all data other than COVID-19 were classified into all different categories. Covid-19 misdiagnosed 34 medical images out of 708 test data in the classification study.

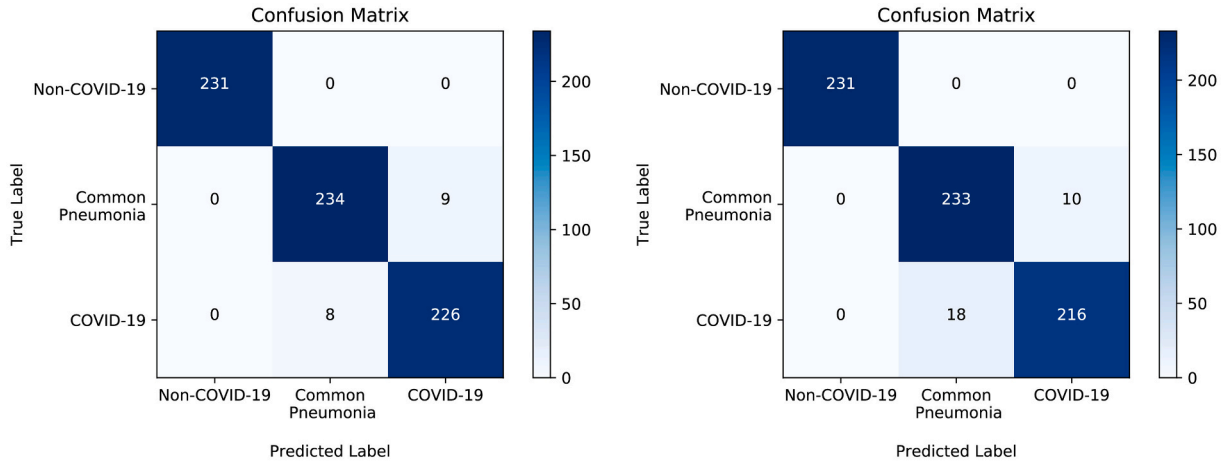

Fig. 10. **(a)** Confusion matrix of COVID-DSNet on COVID-19 and common pneumonia chest CT test dataset **(b)** Confusion matrix of DenseNet169 on COVID-19 and common pneumonia chest CT test dataset.

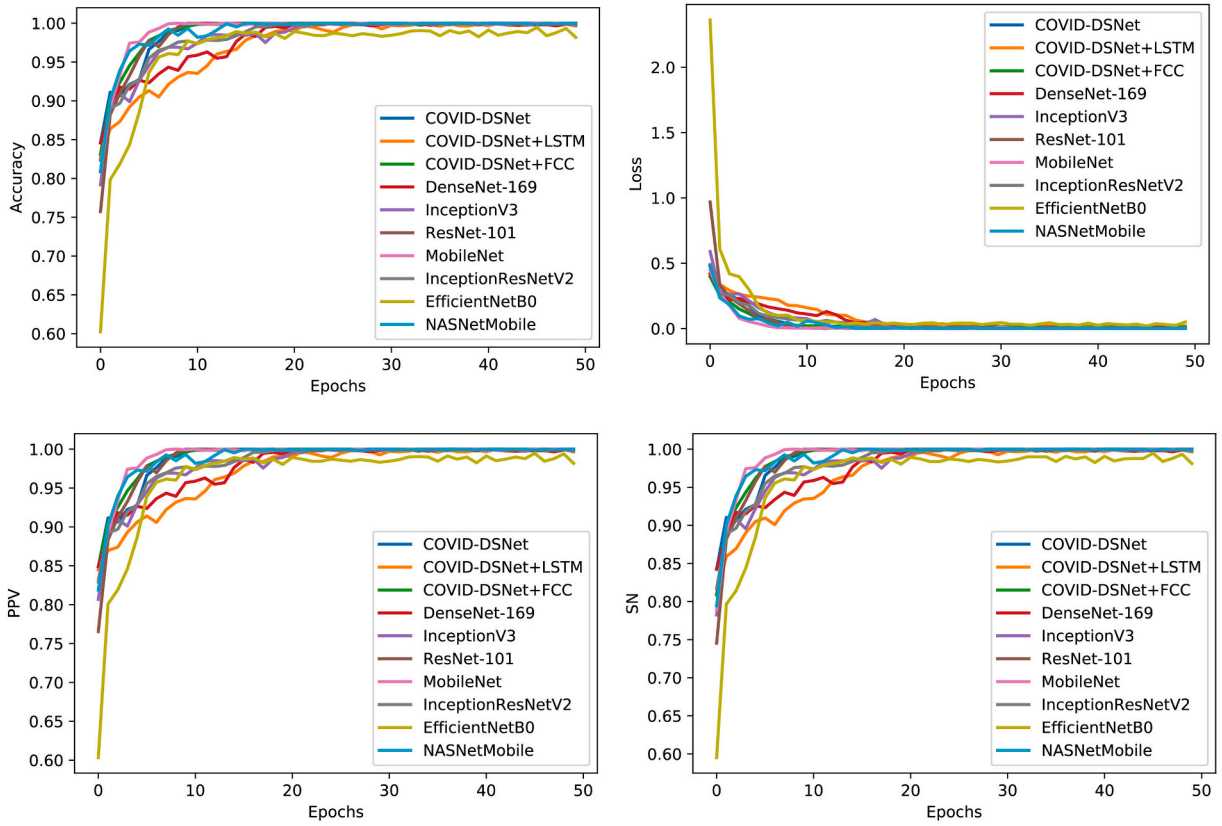

Fig. 11. Graphics of deep neural network architectures on COVID-19 and common pneumonia chest CT train dataset.

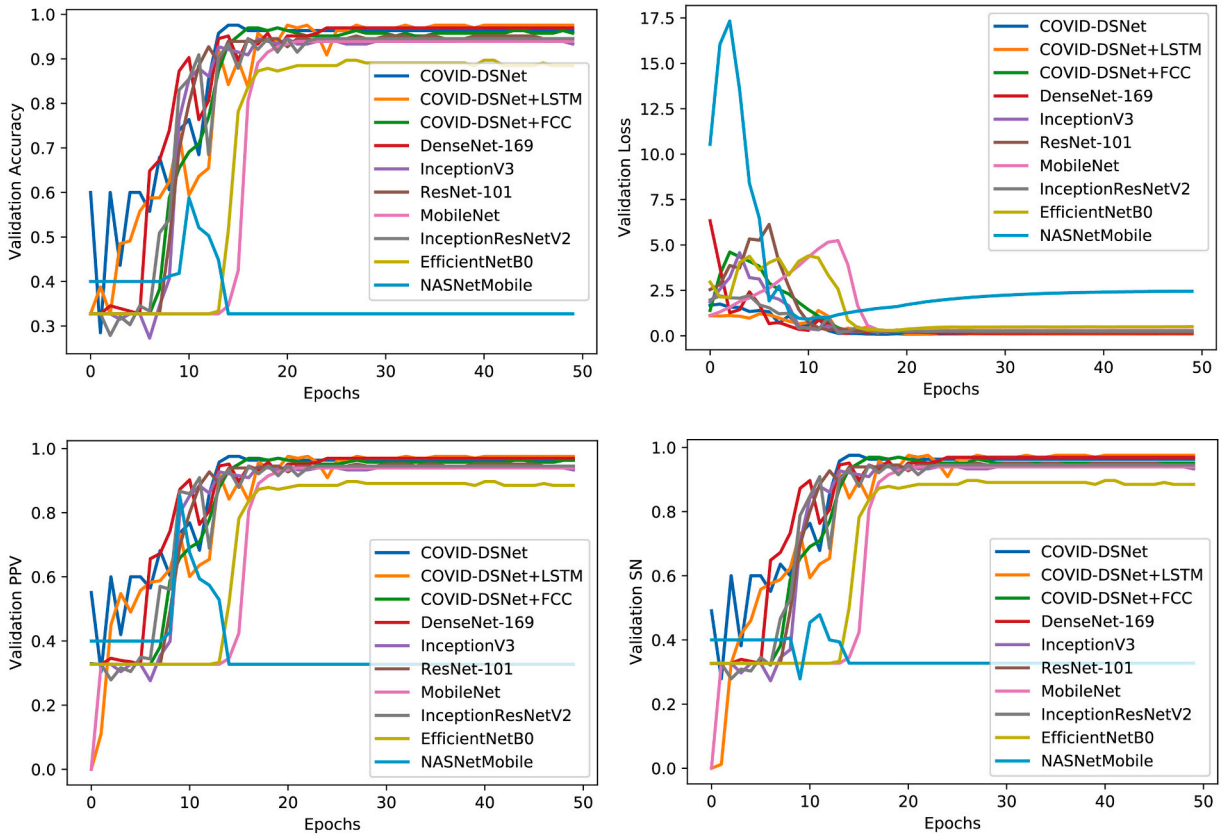

Fig. 12. Graphics of deep neural network architectures on COVID-19 and common pneumonia chest CT validation dataset.

Table 14
Covid19 detection with COVID-DSNet and improved COVID-DSNet models (with train-validation-test split approach).

Method	Params (M)	ACC (%)	Kappa (%)
COVID-DSNet-w/concat	2.57	96.19	94.28
COVID-DSNet-w/add1–2-3	4.16	96.75	95.13
COVID-DSNet-w/conv1–2–3-4	0.83	93.70	90.68
COVID-DSNet-w/transition layer	1.13	95.48	93.22
COVID-DSNet (version 2)	4.19	96.05	94.07
COVID-DSNet	4.17	97.60	96.40

5.1.3. 5-Fold cross-validation performance

A 5 fold cross-validation method was applied to evaluate the classification success of the COVID-DSNet architecture. The 5-fold cross-validation application used a dataset consisting of three-class non-covid19/common pneumonia/covid-19 categories and two-class common pneumonia/covid-19 categories. In the COVID-DSNet architecture triple classification study, the accuracy was 96.05 % in Fold 1, 96.89 % in Fold 2, 95.76 % in Fold 3, 94.21 % in Fold 4, and 95.76 % in Fold 5 (Table 16). The loss and accuracy graphs of deep neural network architectures on 3-class using the Fold-1-5 chest CT train and validation dataset are given in Fig. 15.

5.2. Performance results on chest CXR image dataset

Multi-class (triple and quadruple) and binary (binary) classification was made with the chest X-ray dataset consisting of four categories: Normal, Bacterial Pneumonia, Viral Pneumonia, COVID-19. In the 4-class classification problem, the proposed COVID-DSNet, COVID-DSNet + FCC, COVID-DSNet + LSTM architectures and deep convolutional neural networks InceptionResNetV2, InceptionV3, MobileNet, ResNet-101, DenseNet-169, NASNetMobile, EfficientNetB0 algorithms were applied. The proposed COVID-DSNet architecture has been applied in the 3-class and 2-class classification problems. In the multi-class and binary classification problem, 70 % of the dataset consisting of CXR medical images is divided into training (10 % of the training dataset was used for the validation dataset) and 30 % as the test dataset. In the 4-class classification problem, While 1760 data were used in the training of the models, 755 data were used in the testing process of the models. According to the experimental results, COVID-DSNet was the most successful model in the 4-class classification problem with the chest X-ray dataset. In the multi-class classification problem; While the COVID-DSNet architecture predicts with 88.34 % accuracy; InceptionResNetV2, InceptionV3, MobileNet, ResNet-101, DenseNet-169, NASNetMobile, EfficientNetB0, COVID-DSNet + LSTM, and COVID-DSNet + FCC networks 87.55 %, 87.81 %, 83.97 %, 85.30 %, 87.28 %, 28.48 %, respectively. It estimated 79.87 %, 80.40 %, 87.68 %, and 88.34 % accuracy (Table 17). COVID-DSNet architecture While 90.24 %, 78.02 %, 91.07 %, and 93.50 % experimental results were obtained in the diagnosis of Normal, Bacterial Pneumonia, Viral Pneumonia, and COVID-19, respectively, according to the PPV performance criteria; Second best architecture in chest X-ray dataset 4-class problem InceptionV3 architecture Experimental results of 88.37 %, 79.10 %, 90.06 %, and 93.07 % were obtained in the diagnosis of Normal, Bacterial pneumonia, Viral pneumonia, and COVID-19 according to PPV success criteria, respectively. PPV and SN values obtained from deep learning networks are given as column graphs in Figs. 16 and 17, respectively.

In multi-class classification studies, PPV, SN, and F1 performance criteria are calculated according to micro avg., macro avg., and weighted avg. values. Within the scope of the study, COVID-DSNet, COVID-DSNet + FCC, COVID-DSNet + LSTM, InceptionResNetV2, InceptionV3, MobileNet, ResNet-101, DenseNet-169, NASNetMobile,

Table 15
Three and two-class classification reports (with train-validation-test split approach).

Network	Dataset	ACC (%)	PPV (%)	SN (%)	F1 (%)	Kappa (%)
COVID-DSNet	Three (non-covid19/ common pneumonia/ covid-19)	97.60	97.60	97.60	97.60	96.40
	Two (non-covid19/covid-19)	100	100	100	100	100
	Two (common pneumonia/ covid-19)	92.92	92.41	93.19	92.80	85.83
	Two (all others/ covid-19)	95.20	89.37	97.01	93.03	89.38

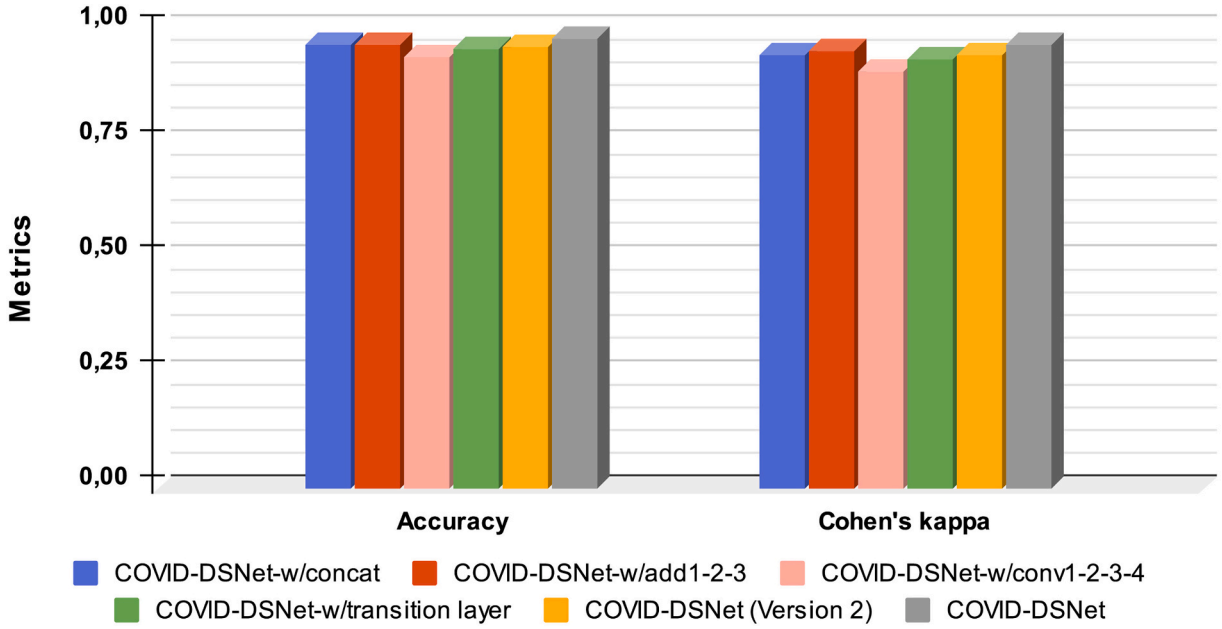

Fig. 13. Covid19 detection with COVID-DSNet and improved COVID-DSNet models.

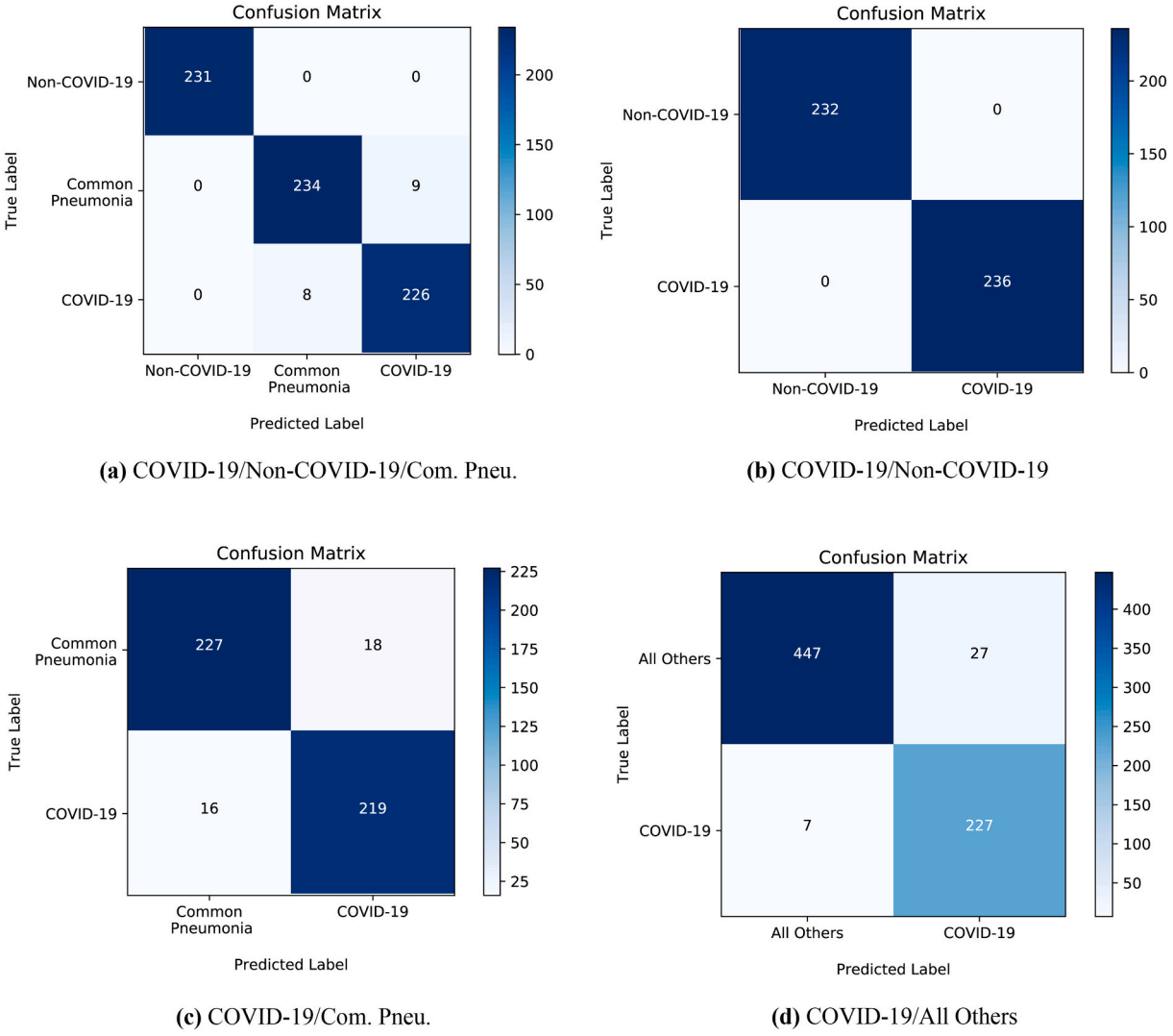

(a) COVID-19/Non-COVID-19/Com. Pneu. **(b)** COVID-19/Non-COVID-19

(c) COVID-19/Com. Pneu. **(d)** COVID-19/All Others

Fig. 14. Confusion matrix of three and two-class classification.

Table 16
Performance of the proposed model (COVID-DSNet) on 5-fold cross-validation using three and two class categories.

Network	Class	Fold	ACC (%)	PPV (%)	SN (%)	Kappa (%)
COVID-DSNet	Three (non-covid19/ common pneumonia/ covid-19)	Fold 1	96.05	96.07	96.05	94.07
		Fold 2	96.89	96.89	96.89	95.34
		Fold 3	95.76	95.77	95.76	93.64
		Fold 4	94.21	94.24	94.21	91.31
		Fold 5	95.76	95.77	95.76	93.64
		Average	95.73	95.75	95.73	93.60
COVID-DSNet	Two (common pneumonia/ covid-19)	Fold 1	91.67	88.24	95.74	83.36
		Fold 2	94.37	93.70	94.89	88.75
		Fold 3	92.29	90.24	94.47	84.59
		Fold 4	93.13	92.08	94.04	86.25
		Fold 5	92.50	90.28	94.89	85.01
		Average	92.79	90.91	94.81	85.59

and EfficientNetB0 applied in the detection of Normal, Bacterial Pneumonia, Viral Pneumonia, and COVID-19 PPV, SN, and F1 performance criteria of the networks were calculated according to micro, macro, and weighted values and the analysis results are given in Table 18. PPV_{micro}, PPV_{macro}, and $PPV_{weighted}$ metric results of the COVID-DSNet architecture were 88.34 %, 88.21 %, 88.80 %, respectively; The PPV_{micro}, PPV_{macro}, and $PPV_{weighted}$ metric results of the InceptionV3 architecture were 87.81 %, 87.65 %, 88.15 %, respectively; The PPV_{micro}, PPV_{macro}, and $PPV_{weighted}$ metric results of the MobileNet architecture are 83.97 %, 83.70 %, 84.22 %, respectively.

The confusion matrix of COVID-DSNet and InceptionV3 networks is given in Fig. 18. In Fig. 19, loss, accuracy, validation loss, and validation accuracy graphs of deep neural networks trained on the Chest X-Ray dataset.

According to Fig. 18, in the multi-class study with the chest CT dataset, the COVID-DSNet architecture, the most successful model, misdiagnosed 88 medical images from 755 test data. In contrast, the second-best architecture, InceptionV3, misdiagnosed 92 medical images from 755 test data.

5.2.1. Binary and multi-class classification with COVID-DSNet architecture

Chest X-Ray dataset consists of four categories: Normal, Bacterial Pneumonia, Viral Pneumonia, COVID-19. For the dataset consisting of Chest X-Ray images to be applied to the triple and binary classification study, the categories in the dataset are normal/viral/covid-19, normal/bacterial/covid-19, bacterial/viral/covid-19, normal/covid-19, viral/Organized as covid-19, bacterial/covid-19, all others/covid-19. The COVID-DSNet architecture was used to classify the three-class categories and the two-class categories. The COVID-DSNet architecture produced 88.34 % accuracy in the quadruple (normal/bacterial/viral/covid-19) classification study. Using the normal/bacterial/covid-19 categories

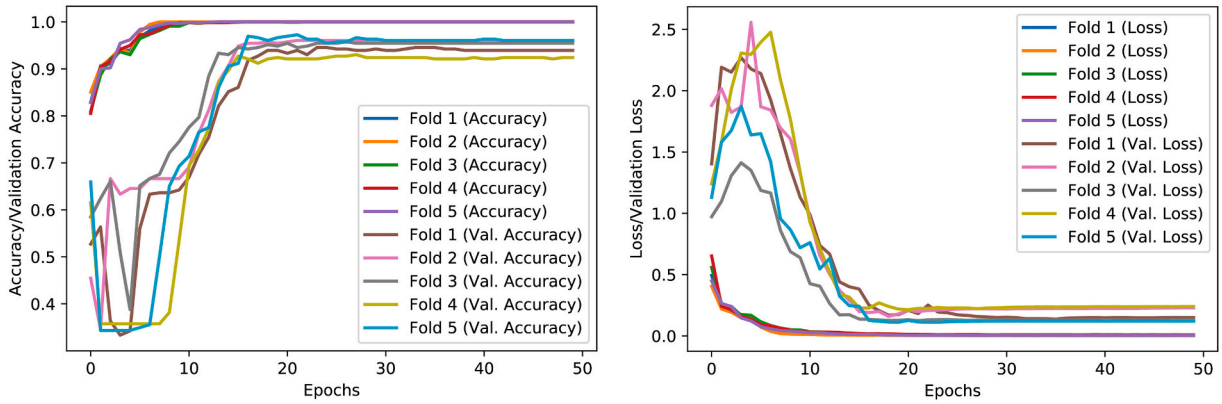

Fig. 15. Loss and accuracy graphics of deep neural network architectures on 3-class using fold-1-5 COVID-19 and common pneumonia chest CT train and validation dataset.

Table 17
Performance of all deep neural network architectures on Chest X-Ray Images (Pneumonia) + COVID-19 Radiography Database test dataset (with train-validation-test split approach). ACC (%), Kappa (%), PPV (%), SN (%), F_1 (%).

Network	Class	ACC	Kappa	PPV	SN	F_1
InceptionResNetV2	Normal	87.55	83.34	92.59	86.63	89.51
	Bacterial pneumonia			82.32	85.99	84.11
	Viral pneumonia			87.57	82.01	84.70
	COVID-19			87.11	94.69	90.74
InceptionV3	Normal	87.81	83.72	88.37	94.06	91.13
	Bacterial pneumonia			79.10	89.17	83.83
	Viral pneumonia			90.06	76.72	82.86
	COVID-19			93.07	90.82	91.93
MobileNet	Normal	83.97	78.59	85.44	87.13	86.27
	Bacterial pneumonia			75.57	84.71	79.88
	Viral pneumonia			84.21	76.19	80.00
	COVID-19			89.60	87.44	88.51
ResNet-101	Normal	85.30	80.33	89.01	84.16	86.51
	Bacterial pneumonia			82.69	82.17	82.43
	Viral pneumonia			81.73	85.19	83.42
	COVID-19			87.20	88.89	88.04
DenseNet-169	Normal	87.28	82.99	91.88	89.60	90.73
	Bacterial pneumonia			82.10	84.71	83.39
	Viral pneumonia			83.98	80.42	82.16
	COVID-19			89.77	93.24	91.47
NASNetMobile	Normal	28.48	01.52	49.06	12.87	20.39
	Bacterial pneumonia			0	0	0
	Viral pneumonia			0	0	0
	COVID-19			26.92	91.30	41.58
EfficientNetB0	Normal	79.87	73.11	79.07	84.16	81.53
	Bacterial pneumonia			72.53	84.08	77.88
	Viral pneumonia			81.48	69.84	75.21
	COVID-19			86.22	81.64	83.87
COVID-DSNet + LSTM	Normal	80.40	73.81	77.53	87.13	82.05
	Bacterial pneumonia			75.27	89.17	81.63
	Viral pneumonia			88.41	64.55	74.62
	COVID-19			82.84	81.64	82.24
COVID-DSNet + FCC	Normal	87.68	83.53	92.11	86.63	89.29
	Bacterial pneumonia			81.50	89.81	85.45
	Viral pneumonia			90.06	81.48	85.56
	COVID-19			86.88	92.75	89.72
COVID-DSNet	Normal	88.34	84.44	90.24	91.58	9091
	Bacterial pneumonia			78.02	90.45	8378
	Viral pneumonia			91.07	80.95	8571
	COVID-19			93.50	90.34	9189

dataset, 93.74 % accuracy was obtained in the triple classification study with the COVID-DSNet architecture. Using the dataset consisting of bacterial/covid-19 categories, 99.45 % accuracy was achieved in the binary classification study with the COVID-DSNet architecture (Table 19). The complex matrix of the binary, triple and quadruple classification study with the COVID-DSNet architecture is given in Fig. 20.

According to Fig. 20, the triple (non-covid19/common pneumonia/covid-19) classification study with the COVID-DSNet architecture misdiagnosed 88 medical images from 755 test data. In comparison, the triple (non-covid19/common pneumonia/covid-19) classification study made with the architecture normal/bacterial/covid-19 misdiagnosed 36 medical images from 575 test data in the classification study and finally misdiagnosed two medical images from 365 test data in the dual classification study of COVID-19 Bacterial/covid-19.

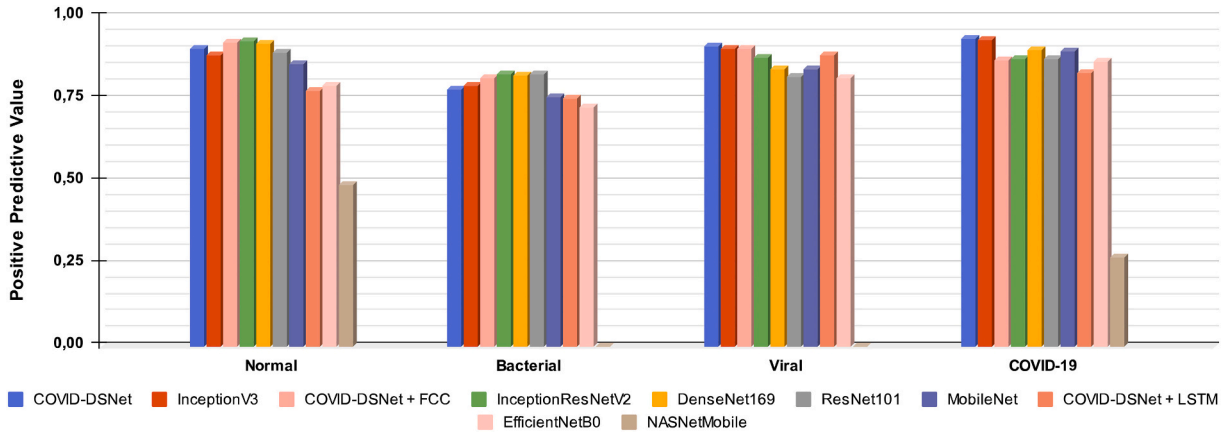

Fig. 16. Graphical analysis of model performance using deep neural network architectures (with PPV metrics).

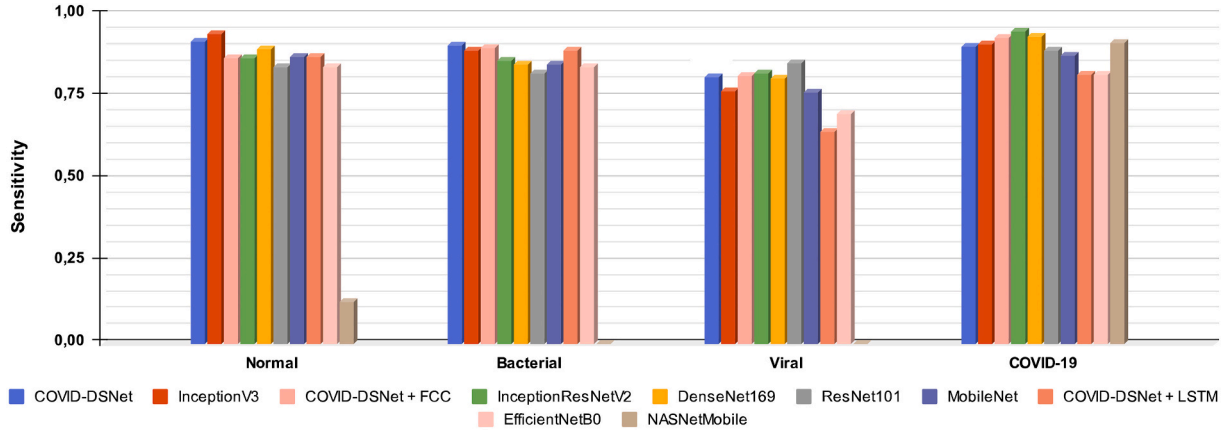

Fig. 17. Graphical analysis of model performance using deep neural network architectures (with SN metrics).

Table 18
Empirical results of $PPV_{micro,\ macro,\ weighted}$ (%), $SN_{micro,\ macro,\ weighted}$ (%), and $F1_{micro,\ macro,\ weighted}$ (%) performance metrics of deep learning Algorithms (with train-validation-test split approach). Avg 1: Micro, Avg 2: Macro, Avg 3: Weighted.

Network	PPV			SN			F_1		
	Avg1	Avg2	Avg3	Avg1	Avg2	Avg3	Avg1	Avg2	Avg3
InceptionResNetV2	87.55	87.40	87.70	87.55	87.33	87.55	87.55	87.27	87.52
InceptionV3	87.81	87.65	88.15	87.81	87.69	87.81	87.81	87.44	87.76
MobileNet	83.97	83.70	84.22	83.97	83.87	83.97	83.97	83.67	83.99
ResNet-101	85.30	85.16	85.38	85.30	85.10	85.30	85.30	85.10	85.31
DenseNet-169	87.28	86.93	87.29	87.28	86.99	87.28	87.28	86.94	87.26
NASNetMobile	28.48	None	20.51	28.48	26.04	28.48	28.48	15.49	16.86
EfficientNetB0	79.87	79.83	80.27	79.87	79.93	79.87	79.87	79.62	79.83
COVID-DSNet + LSTM	80.40	81.01	81.24	80.40	80.62	80.40	80.40	80.13	80.15
COVID-DSNet + FCC	87.68	87.64	87.95	87.68	87.67	87.68	87.68	87.50	87.67
COVID-DSNet	88.34	88.21	88.80	88.34	88.33	88.34	88.34	88.07	88.39

5.2.2. 5-Fold cross-validation performance

A 5 fold cross-validation method was applied to evaluate the classification success of the COVID-DSNet architecture. In the 5-fold cross-validation application, the dataset consisting of four-class normal/bacterial/viral/covid-19 categories, three-class bacterial/viral/covid-19 categories, and two-class viral/covid-19 categories were used. In the COVID-DSNet architecture binary classification study, 99.49 % accuracy was obtained in Fold 1, 99.49 % in Fold 2, 99.49 % in Fold 3, 99.23 % in Fold 4, and 100 % in Fold 5 (Table 20). Loss and accuracy graphics of deep neural network architectures on 2-class using fold-1-5 chest X-Ray train and validation dataset (Fig. 21).

5.3. Performance results on chest CT + CXR image dataset

In the study, the hybrid CT + CXR dataset compiled with CT and CXR images consists of Non-COVID-19 and COVID-19 categories. In the binary classification study with the hybrid CT + CXR dataset, the proposed COVID-DSNet, COVID-DSNet + FCC, COVID-DSNet + LSTM architectures were applied.

In binary classification with hybrid CT + CXR dataset, COVID-DSNet architecture 95.42 %, COVID-DSNet + FCC architecture 95.69 % achieved accuracy (Table 21).

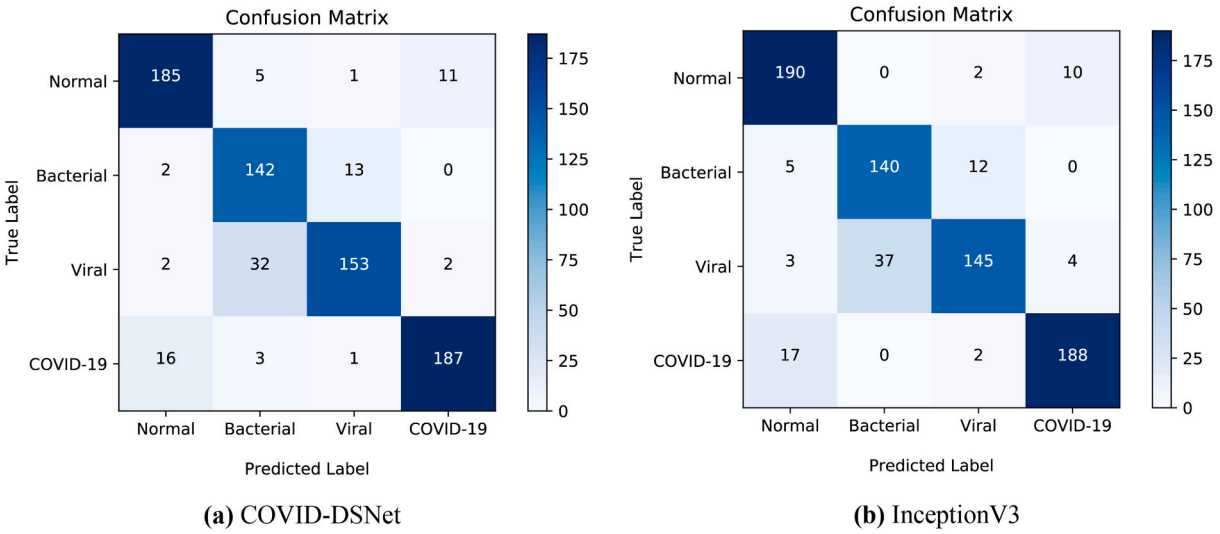

Fig. 18. (a) Confusion matrix of COVID-DSNet on Chest X-Ray Images (Pneumonia) + COVID-19 Radiography Database test dataset (b) Confusion matrix of InceptionV3 on Chest X-Ray Images (Pneumonia) + COVID-19 Radiography Database test dataset.

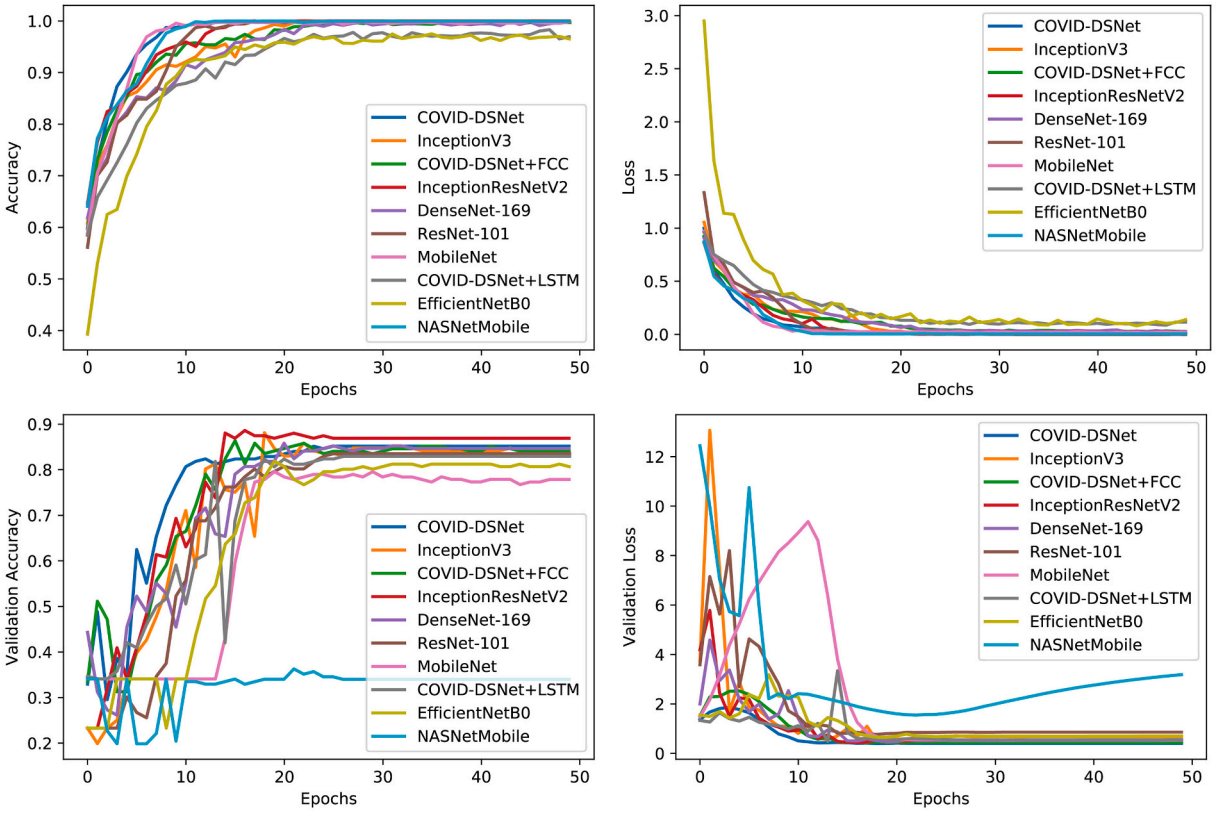

Fig. 19. Evaluation results of all deep neural network architectures on Chest X-Ray Images (Pneumonia) + COVID-19 Radiography Database train dataset and validation dataset.

5.3.1. 5-Fold cross-validation performance

A 5 fold cross-validation method was applied to evaluate the classification success of COVID-DSNet, COVID-DSNet + FCC, COVID-DSNet + LSTM architectures. In the 5-fold cross-validation application, the accuracy was 95.56 % in COVID-DSNet + FCC Fold 1, 95.14 % in Fold 2, 95.56 % in Fold 3, 95.83 % in Fold 4, and 95.56 % in Fold 5 (Table 22).

5.4. Comparison of the results obtained with the proposed method with the latest technological methods in the literature

In this section, by creating dual, triple, and quadruple class categories, using CT and chest X-ray medical images, experimental results of the latest technological methods suggested in the literature for the early detection of normal, pneumonia, COVID-19 cases and proposed COVID-DSNet, COVID-DSNet + FCC, COVID-DSNet + LSTM comparative analysis of experimental results of architectures are given in Table 23.

Table 19
Four, three, and two-class classification reports (with train-validation-test split approach).

Network	Dataset	ACC (%)	PPV (%)	SN (%)	F1 (%)	Kappa (%)
COVID-DSNet	Four (normal/bacterial/viral/covid-19)	88.34	88.80	88.34	88.39	84.44
	Three (normal/viral/covid-19)	92.83	92.88	92.83	92.81	89.21
	Three (normal/bacterial/covid-19)	93.74	93.75	93.74	93.74	90.50
	Three (bacterial/viral/covid-19)	87.71	87.81	87.71	87.65	81.44
	Two (normal/covid-19)	94.76	94.84	94.84	94.84	89.52
	Two (viral/covid-19)	98.97	100	98.13	99.06	97.93
	Two (bacterial/covid-19)	99.45	99.55	99.55	99.55	98.85
	Two (all others/covid-19)	94.97	94.71	86.47	90.40	87.00

Table 20
Performance of the proposed model (COVID-DSNet) on 5-fold cross-validation using four, three, and two-class categories.

Network	Class	Fold	ACC (%)	PPV (%)	SN (%)	Kappa (%)
COVID-DSNet	Four (normal/bacterial/viral/covid-19)	Fold 1	89.40	89.70	89.40	85.85
		Fold 2	87.42	87.86	87.42	83.20
		Fold 3	86.49	86.78	86.49	81.96
		Fold 4	89.01	89.36	89.01	85.32
		Fold 5	86.36	86.57	86.36	81.76
		Average	87.74	88.05	87.74	83.62
COVID-DSNet	Three (bacterial/viral/covid-19)	Fold 1	90.64	90.90	90.64	85.92
		Fold 2	90.64	90.60	90.64	85.90
		Fold 3	86.42	86.93	86.42	79.47
		Fold 4	90.28	90.24	90.28	85.35
		Fold 5	90.83	90.90	90.83	86.15
		Average	89.76	89.91	89.76	84.56
COVID-DSNet	Two (viral/covid-19)	Fold 1	99.49	99.07	100	98.96
		Fold 2	99.49	99.07	100	98.96
		Fold 3	99.49	99.53	99.53	98.96
		Fold 4	99.23	98.62	100	98.44
		Fold 5	100	100	100	100
		Average	99.54	99.26	99.91	99.07

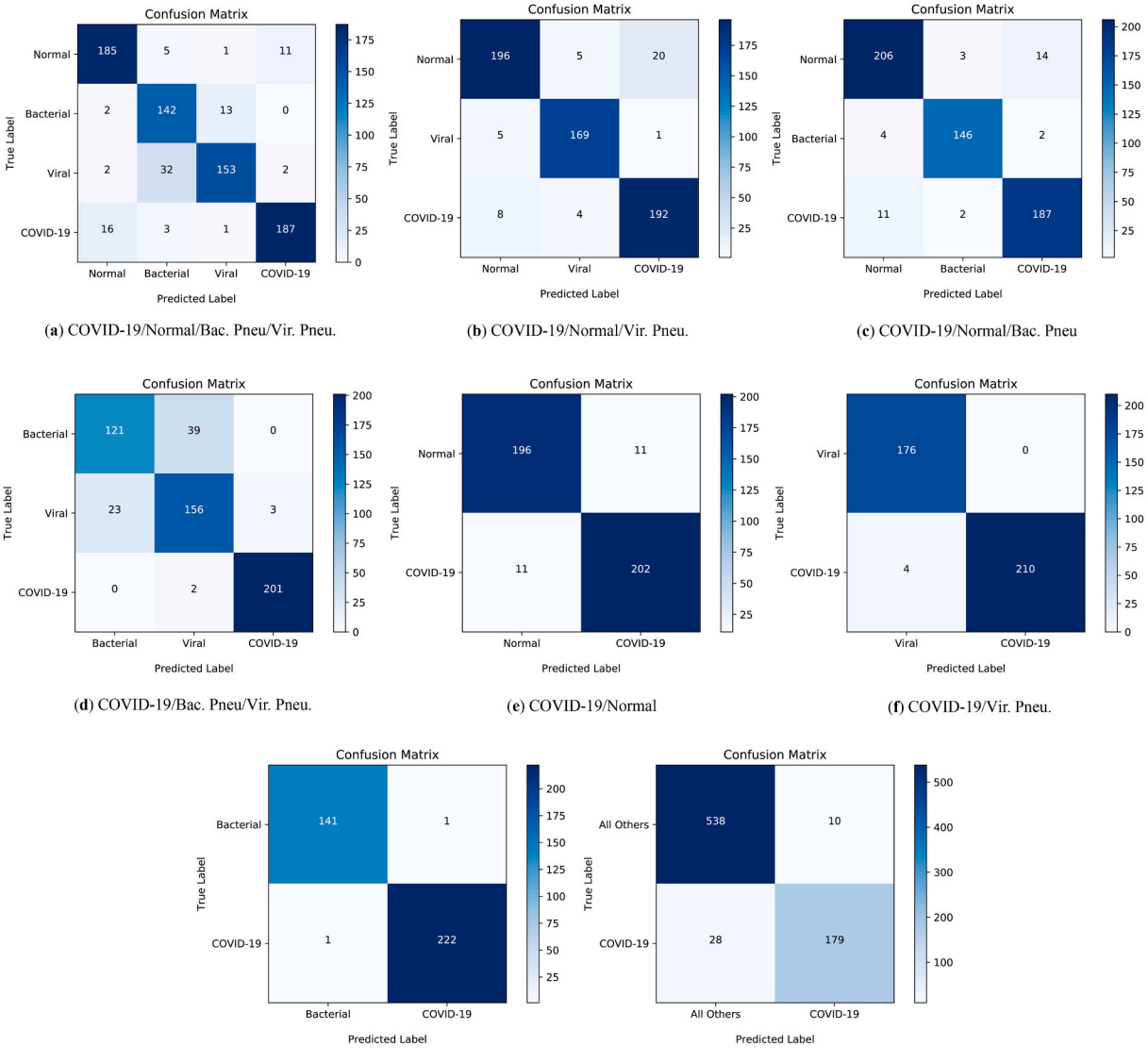

(a) COVID-19/Normal/Bac. Pneu/Vir. Pneu.
(b) COVID-19/Normal/Vir. Pneu.
(c) COVID-19/Normal/Bac. Pneu
(d) COVID-19/Bac. Pneu/Vir. Pneu.
(e) COVID-19/Normal
(f) COVID-19/Vir. Pneu.
(g) COVID-19/Bac. Pneu.
(h) COVID-19/All Others

Fig. 20. Confusion matrix of four, three, and two-class classification.

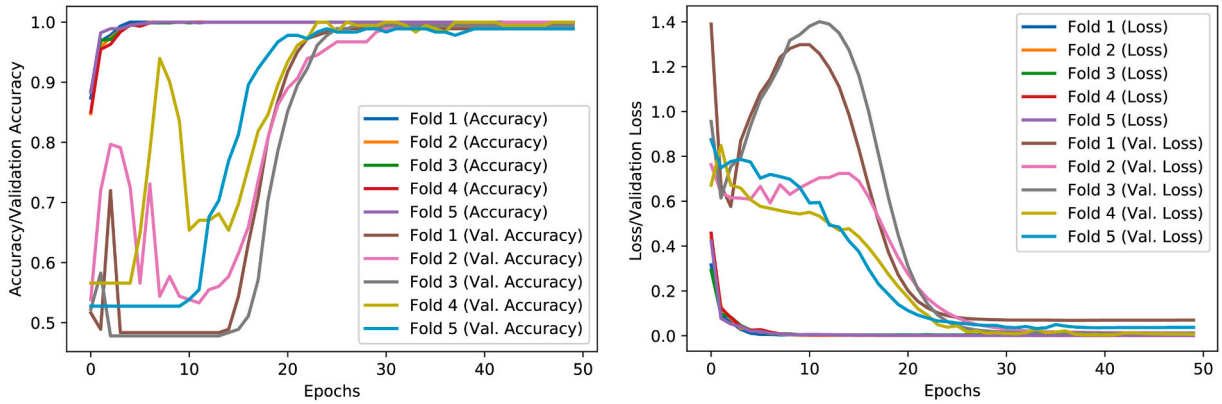

Fig. 21. Loss and accuracy graphics of deep neural network architectures on 2-class using fold-1-5 Chest X-Ray Images (Pneumonia) + COVID-19 Radiography Database.

Table 21
Performance of all deep neural network architectures on Chest X-Ray Images (Pneumonia) + COVID-19 Radiography Database test dataset (with train-validation-test split approach).

Network	ACC (%)	PPV (%)	SN (%)	F1-score (%)	Cohen's Kappa (%)
COVID-DSNet + LSTM	94.17	93.75	94.29	94.02	88.33
COVID-DSNet + FCC	95.69	94.68	96.57	95.62	91.39
COVID-DSNet	95.42	93.19	97.71	95.40	90.84

Table 22
Performance of the proposed models on 5-fold cross-validation using two (non-covid19/covid-19) class categories.

Network	Fold	ACC (%)	PPV (%)	SN (%)	Kappa (%)
COVID-DSNet + LSTM	Fold 1	89.00	89.47	93.70	75.85
	Fold 2	92.50	92.42	96.06	83.58
	Fold 3	88.50	89.39	92.91	74.82
	Fold 4	90.50	90.91	94.49	79.20
	Fold 5	88.50	88.81	93.70	74.68
	Average	89.80	90.20	94.17	77.63
COVID-DSNet + FCC	Fold 1	95.56	95.69	95.14	91.10
	Fold 2	95.14	94.87	95.14	90.27
	Fold 3	95.56	96.22	94.57	91.10
	Fold 4	95.83	96.24	95.14	91.66
	Fold 5	95.56	96.22	94.57	91.10
	Average	95.53	95.85	94.91	91.05
COVID-DSNet	Fold 1	95.28	94.38	96.00	90.55
	Fold 2	95.56	96.76	94.00	91.10
	Fold 3	94.17	92.78	95.43	88.33
	Fold 4	95.97	94.96	96.86	91.94
	Fold 5	95.69	94.93	96.29	91.39
	Average	95.33	94.76	95.71	90.66

6. Discussion

In addition to the serious negative effects of SARS-CoV-2 infection on human health, it has turned into a global crisis by negatively affecting many areas such as the economy, education, and tourism, especially the health system [27]. The SARS-CoV-2 virus can cause serious health problems in people with chronic health problems, the elderly, and in patients with weakened immune systems. The SARS-CoV-2 virus causes serious pathologies in many organs and tissues such as the heart, brain, kidney, and especially lung [32]. In a study conducted at the University Hospital in Frankfurt, Germany, myocarditis (inflammation of the heart muscle) was observed in 60 of 100 patients who recovered from SARS-CoV-2 infection [41]. In their study at the University of Oxford, England, Douaud et al. [99] a reduction in the brain volume was observed in patients with COVID-19 infection. The study examined MRI scans of 401 patients who had COVID-19 and 384 (control group) patients who were not infected with COVID-19. As a result, In patients with SARS-CoV-2 infection, (i) reduction in the whole brain volume of 0.2 %–2 %, (ii) reduction in gray matter in the parahippocampal gyrus and orbitofrontal cortex, and (iii) brain tissue damage in regions connected to the olfactory cortex were observed. SARS-CoV-2 underwent various mutations over time, and mutations in the virus significantly increased the transmission rate [50,52]. Due to the rapid spread of the disease and the severe clinical picture resulting from the infection, rapid detection of infected people is critical in preventing the spread of the disease. Computed Tomography (CT) and chest X-ray (CXR) medical imaging methods are frequently used to detect the disease [56]. In the clinical picture resulting from SARS-CoV-2 infection, abnormalities such as GGO and consolidative pulmonary opacity were observed in the lungs of infected patients. Due to the significant differences in virus-infected and uninfected patients, convolutional neural networks (CNNs) with high discriminating power and high processing power have become a popular solution technique in the disease detection process. As far as we can research, it has been observed that most of the studies in the literature are carried out with architectures developed with Conv Layer (Conv2D). To improve the classification success of deep neural networks, the depth of their architecture is often increased. However, as the depth of the architectures developed with the Convolution layer (CONV) increases, the problem of gradient disappearance is encountered. In addition, the increase in the use of the convolution layer in architecture causes an increase in the number of parameters and an increase in cost. Here, depthwise separable convolution, a promising technology, can be used to reduce the processing volume compared to the standard convolution layer (CONV Layer) and has a high processing capacity with fewer parameters. The proposed COVID-DSNet in this study is a deep convolutional neural network architecture based on depthwise convolution and separable convolution. The proposed COVID-DSNet architecture has been developed with an approach that includes residual networks and additional feature vectors to avoid the gradient loss/information loss problem experienced in hierarchical feed-forward neural networks. The majority of COVID-19 studies have focused on using high-parameter deep neural networks. Here, the success of high-capacity architectures depends on big data. In addition, the diagnostic time of high-parameter deep neural networks is long. The model proposed in this study is a deep neural network with relatively few parameters, and it can be an alternative solution with additional feature vectors in COVID-19 detection studies. Architectural datasets are trained and tested from scratch. A transfer learning technique focused on pre-trained networks can be applied to improve the success of networks from scratch. ImageNet dataset transfer learning technique can improve the classification

Table 23
Four, three, and two class performance comparison of the proposed method with the state of art methods.

Literature	Imaging modality	Models	Dataset	Performance
Tahir et al. [71]	Chest X-Ray	Pretrained deep CNNs (InceptionV3, DenseNet201, SqueezeNet, and ResNet18)	QU-COVID (SARS-CoV, MERS-CoV, and Covid-19) Dataset	Sensitivity of 99.5 % for 3-classes
Khan et al. [72]	Chest X-Ray	Pretrained deep CNNs (EfficientNetB1, NasNetMobile, and MobileNetV2)	4-way (Normal, lung opacity, pneumonia, and Covid-19) Dataset	Accuracy of 96.13 % for 4-classes
Chouat et al. [73]	CT + Chest X-Ray	Pretrained deep CNNs (InceptionV3, ResNet50, Xception, and VGGNet-19)	2-Way (normal, Covid-19) CT Dataset	Accuracy of 87.0 % for 2-classes
			2-Way (normal, Covid-19) Chest X-Ray Dataset	Accuracy of 98.0 % for 2-classes
Kundu et al. [74]	CT	ET-NET Bagging ensemble classifier	2-Way (non-Covid-19, Covid-19) Dataset	Accuracy of 97.81 % for 2-classes
Wang et al. [75]	Chest X-Ray	COVID-Net	COVIDx (3-way (Normal, non-Covid-19 [e.g., viral, bacterial, etc.], and Covid-19))	Accuracy of 93.30 % for 3-classes
Kumar et al. [77]	Chest X-Ray	SARS-Net	3-Way (Normal, non-Covid-19 [e.g., viral, bacterial, etc.], and Covid-19) Dataset	Accuracy of 97.60 % for 3-classes
Li et al. [79]	CT	COVNet	3-Way (Non-pneumonia, community-acquired pneumonia, and Covid-19) Dataset	Sensitivity of 90.00 % for 3-classes
Chandra et al. [95]	Chest X-Ray	Majority vote based classifier ensemble	3-Way (Normal, pneumonia, and Covid-19) Dataset	Accuracy of 93.41 % for 3-classes
Gayathri et al. [96]	Chest X-Ray	Pre-trained model (InceptionResnetV2 + Xception)	2-Way (non-Covid-19, Covid-19) Dataset	Accuracy of 95.78 % for 2-classes
Loey et al. [97]	Chest X-Ray	CNN Model	3-Way (Normal, pneumonia, and Covid-19) Dataset	Accuracy of 96.00 % for 2-classes
Li et al. [98]	CT	The modified CheXNet	2-way (non-Covid-19, Covid-19) Dataset	Accuracy of 87.00 % for 2-classes
Proposed Method I	CT + Chest X-Ray	COVID-DSNet	4-Way (normal, bacterial pneumonia, viral pneumonia, Covid-19) Chest X-Ray Dataset	Accuracy of 88.34 % for 4-classes
			3-Way (normal, viral pneumonia, Covid-19) Chest X-Ray Dataset	Accuracy of 92.83 % for 3-classes
			2-Way (bacterial pneumonia, Covid-19) Chest X-Ray Dataset	Accuracy of 99.45 % for 2-classes
			3-Way (non-Covid-19, common pneumonia, Covid-19) CT Dataset	Accuracy 97.60 % for 3-classes
			2-Way (non-Covid-19, Covid-19) CT Dataset	Accuracy 100 % for 2-classes
Proposed Method II	CT + Chest X-Ray	COVID-DSNet + LSTM	4-Way (normal, bacterial pneumonia, viral pneumonia, Covid-19) Chest X-Ray Dataset	Accuracy of 80.40 % for 4-classes
			3-Way (non-Covid-19, common pneumonia, Covid-19) CT Dataset	Accuracy of 96.33 % for 3-classes
Proposed Method III	CT + Chest X-Ray	COVID-DSNet + FCC	4-Way (normal, bacterial pneumonia, viral pneumonia, Covid-19) Chest X-Ray Dataset	Accuracy of 87.68 % for 4-classes
			3-Way (non-Covid-19, common pneumonia, Covid-19) CT Dataset	Accuracy of 96.19 % for 3-classes

success of the proposed architecture. The empirical results show that the datasets consisting of architectural CT, CXR, and hybrid CT + CXR medical images produced successful results in binary and multi-class studies. The proposed COVID-DSNet produced successful binary and multi-class classification results in the experimental analyses performed with the CT dataset. However, the noisy and technically incorrect data in the CT dataset negatively affected the learning process of the architecture. Although it had an acceptable success in the 4-class classification study in the CXR dataset, the model's training was negatively affected due to insufficient data for each category due to the lack of technical equipment. The model produced successful results in binary classification, well above expectations.

7. Conclusions and future work

Performance analysis was carried out by testing the proposed

architectural datasets consisting of CT and chest X-ray medical images and train-validation-test split approach and k-fold methods. According to the experimental results, it can be said that the proposed approach is effective. Early detection of COVID-19 can prevent severe pathological problems. The importance of treatment and diagnosis methods in medicine in the diagnosis process of the disease cannot be denied. However, we believe that deep neural networks will contribute to and benefit the disease detection process. COVID-DSNet is a practically deep convolutional neural network architecture with fewer parameters than modern architectures that can reduce the cost by reducing the processing volume in the computational part. Therefore, data scientists can benefit from and develop. Although the proposed architecture is not a definitive solution, (i) it is expected to assist data scientists in solving the problem of gradient disappearance (ii) may benefit experts in the early diagnosis and diagnosis of COVID-19. In future studies; To increase the efficiency of multi-class studies on the dataset consisting of CT and CXR images, (i) the depth of the proposed model can be increased, (ii) transfer learning can be applied with ImageNet, (iii) data augmentation methods can be applied (generative adversarial network (GAN), variational autoencoder methods can be used to generate new data), (iv) the performance of the architectures can be improved by detecting and removing noisy regions outside the lung sections in CT and CXR images. The proposed study has some limitations. Firstly, due to a lack of technical equipment, the models trained within the scope of the study were trained and tested with a small dataset. Second, the datasets used in the study are in jpeg format. Therefore, these data are lossy. Training and testing can be performed with files with the dicom extension to test the proposed architecture's real-life success.

Finally, in the "COVID-19 and common pneumonia chest CT dataset" dataset, which constitutes the CT dataset in the study, noisy and technically incorrect contents were detected in some of the lung sections in common pneumonia and COVID-19 categories (Fig. 7 (a) Chest CT-scan images). The noisy data in the CT dataset negatively affected the performance of the proposed COVID-DSNet architecture in classification. Although deep neural networks are successful in disease detection, the results still need to be analyzed and interpreted by a specialist doctor for precise %100 accuracy.

CRediT authorship contribution statement

Hatice Catal Reis: Conceptualization, Methodology, Validation, Formal analysis, Investigation, Writing – review & editing. Veysel Turk: Conceptualization, Methodology, Statistics, Software, Writing-editing.

Declaration of competing interest

The authors declare that they have no known competing financial interests or personal relationships that could have appeared to influence the work reported in this paper.

Acknowledgments

None.

Appendix A

Time complexity

In this study, considering the depth of the proposed deep neural network while calculating the time complexity of the COVID-DSNet, COVID-DSNet + FCC, and COVID-DSNet + LSTM architectures proposed in the detection of COVID-19, only the time complexity of the convolutional layers was calculated to reduce the complexity of the computation process. To calculate the time complexity of the proposed architectures, Eq. (22) was used in the time complexity calculation process [100];

$$O = \left\{ \sum_{j=1}^{k} n_{j-1} * s_w * s_h * n_j * m_w * m_h \right\} \tag{22}$$

where j index of the convolution layer, k the number of convolutional layers, n_{j-1} j-1. A number of input channels/filters in the layer, n_j j. the number of output channels/filters in the layer, s_w, s_h width and height of the filters, m_w width of the output feature vectors, m_h height of output feature map.

The time complexity of the proposed architectures, the number of parameters used in the training of deep neural networks, the running times during the training and testing of the architectures are given in Table 24.

Table 24
The trainable params and time complexity of proposed models.

Model	Trainable parameters	Training time	Testing time	Time complexity
COVID-DSNet	4.17 M	2018.38 s	36.62 s	2.5 billion
COVID-DSNet + FCC	4.25 M	1956.05 s	22.79 s	2.5 billion
COVID-DSNet + LSTM	7.34 M	2082.47 s	22.46 s	2.5 billion

While the trainable parameters of the COVID-DSNet architecture are 4.17 M, the trainable parameters of the COVID-DSNet + FCC and COVID-DSNet + LSTM architectures are 4.25 M and 7.34 M, respectively. In the COVID-DSNet architecture, the training period was 2018.38 s, and the testing period was 36.62 s. In the COVID-DSNet + LSTM architecture, the training period was 2082.47 s, and the testing period was 22.46 s. Since the conv layer in the proposed algorithms has the same number of input and output feature maps, the time complexity results of the architectures are equal.

References

[1] Gupta A, Gupta S, Katarya R. InstaCovNet-19: a deep learning classification model for the detection of COVID-19 patients using chest X-ray. Appl Soft Comput 2021;99:106859. https://doi.org/10.1016/j.asoc.2020.106859.

[2] Wu K, Wang D, Wang J, Zhou Y. Translation landscape of SARS-CoV-2 noncanonical subgenomic RNAs. Virol Sin 2022. https://doi.org/10.1016/j.virs.2022.09.003.

[3] Dobrynin D, Polishchuk I, Portal L, Zlotver I, Sosnik A, Pokroy B. Adsorption of SARS CoV-2 spike proteins on various functionalized surfaces correlates with the

high transmissibility of Delta and omicron variants. Mater. Today Bio 2022;14: 100265. https://doi.org/10.1016/j.mtbio.2022.100265.
[4] Takeda M. Proteolytic activation of SARS-CoV-2 spike protein. Microbiol Immunol 2022;66(1):15–23. https://doi.org/10.1111/1348-0421.12945.
[5] Zhu C, He G, Yin Q, Zeng L, Ye X, Shi Y, et al. Molecular biology of the SARs-CoV-2 spike protein: a review of current knowledge. J Med Virol 2021;93(10): 5729–41. https://doi.org/10.1002/jmv.27132.
[6] Harvey WT, Carabelli AM, Jackson B, Gupta RK, Thomson EC, Harrison EM, et al. SARS-CoV-2 variants, spike mutations and immune escape. Nat Rev Microbiol 2021;19(7):409–24. https://doi.org/10.1038/s41579-021-00573-0.
[7] Larkin HD. Antibody found in mice neutralizes SARS-CoV-2 and SARS-CoV-1. JAMA 2022;328(10):916–7. https://doi.org/10.1001/jama.2022.14711.
[8] Zhang G, Cong Y, Liu FL, Sun J, Zhang J, Cao G, et al. A nanomaterial targeting the spike protein captures SARS-CoV-2 variants and promotes viral elimination. Nat Nanotechnol 2022;17:993–1003. https://doi.org/10.1038/s41565-022-01177-2.
[9] Jackson CB, Farzan M, Chen B, Choe H. Mechanisms of SARS-CoV-2 entry into cells. Nat Rev Mol Cell Biol 2022;23(1):3–20. https://doi.org/10.1038/s41580-021-00418-x.
[10] Gusev E, Sarapultsev A, Solomatina L, Chereshnev V. SARS-CoV-2-specific immune response and the pathogenesis of COVID-19. Int J Mol Sci 2022;23(3): 1716. https://doi.org/10.3390/ijms23031716.
[11] Malone B, Urakova N, Snijder EJ, Campbell EA. Structures and functions of coronavirus replication–transcription complexes and their relevance for SARS-CoV-2 drug design. Nat Rev Mol Cell Biol 2022;23(1):21–39. https://doi.org/10.1038/s41580-021-00432-z.
[12] Fang C, Bai S, Chen Q, Zhou Y, Xia L, Qin L, et al. Deep learning for predicting COVID-19 malignant progression. Med Image Anal 2021;72:102096. https://doi.org/10.1016/j.media.2021.102096.
[13] Chrabaszcz K, Kaminska K, Song CL, Morikawa J, Kujdowicz M, Michalczyk E. Fourier transform infrared polarization contrast imaging recognizes proteins degradation in lungs upon metastasis from breast cancer. Cancers 2021;13(2): 162. https://doi.org/10.3390/cancers13020162.
[14] Singh L, Bajaj S, Gadewar M, Verma N, Ansari MN, Saeedan AS, et al. Modulation of host immune response is an alternative strategy to combat SARS-CoV-2 pathogenesis. Front Immunol 2021:12. https://doi.org/10.3389/fimmu.2021.660632.
[15] Ibrahim AU, Ozsoz M, Serte S, Al-Turjman F, Yakoi PS. Pneumonia classification using deep learning from chest X-ray images during COVID-19. Cognitive Computation 2021:1–13. https://doi.org/10.1007/s12559-020-09787-5.
[16] Cui X, Chen W, Zhou H, Gong Y, Zhu B, Lv X, et al. Pulmonary edema in COVID-19 patients: mechanisms and treatment potential. Front Pharmacol 2021;12: 1444. https://doi.org/10.3389/fphar.2021.664349.
[17] Raghav A, Khan ZA, Upadhayay VK, Tripathi P, Gautam KA, Mishra BK, et al. Mesenchymal stem cell-derived exosomes exhibit promising potential for treating SARS-CoV-2-infected patients. Cells 2021;10(3):587. https://doi.org/10.3390/cells10030587.
[18] Rahman A, Tabassum T, Araf Y, Al Nahid A, Ullah M, Hosen MJ. Silent hypoxia in COVID-19: pathomechanism and possible management strategy. Mol Biol Rep 2021;48(4):3863–9. https://doi.org/10.1007/s11033-021-06358-1.
[19] Walter K. Mechanical ventilation. JAMA 2021;326(14):1452. https://doi.org/10.1001/jama.2021.13084. 1452.
[20] Visca D, Migliori GB, Dinh-Xuan AT, Centis R, Belli S, Vitacca M, et al. The role of blood gas analysis in the post-acute phase of COVID-19 pneumonia. Arch. Bronconeumol. 2022;58(6):513. https://doi.org/10.1016/j.arbres.2021.06.003.
[21] Delli Pizzi A, Chiarelli AM, Chiacchiaretta P, Valdesi C, Croce P, Mastrodicasa D, et al. Radiomics-based machine learning differentiates “ground-glass” opacities due to COVID-19 from acute non-COVID-19 lung disease. Sci Rep 2021;11(1): 17237. https://doi.org/10.1038/s41598-021-96755-0.
[22] Valaiyapathi R, Wu MS, McGregor A. Ground glass opacities are not always COVID-19: a case of acute eosinophilic pneumonitis caused by daptomycin. The Lancet 2022;399(10321):270. https://doi.org/10.1016/S0140-6736(22)00009-5.
[23] Behzadi-Khormouji H, Rostami H, Salehi S, Derakhshande-Rishehri T, Masoumi M, Salemi S. Deep learning, reusable and problem-based architectures for detection of consolidation on chest X-ray images. Comput Methods Programs Biomed 2020;185:105162. https://doi.org/10.1016/j.cmpb.2019.105162.
[24] Marini TJ, Rubens DJ, Zhao YT, Weis J, O'Connor TP, Novak WH, et al. Lung ultrasound: the essentials. radiology: cardiothoracic. Imaging 2021;3(2). https://doi.org/10.1148/ryct.2021200564.
[25] Parry AH, Wani AH, Yaseen M, Dar KA, Choh NA, Khan NA, et al. Spectrum of chest computed tomographic (CT) findings in coronavirus disease-19 (COVID-19) patients in India. Eur J Radiol 2020;129:109147. https://doi.org/10.1016/j.ejrad.2020.109147.
[26] Yu H, Wang K, Huang D, Wen L, Zhang Y, Wang Y, et al. Crazy-paving patterns as rare radiological manifestations of pulmonary cryptococcosis: a case report. BMC Pulm Med 2021;21(1):1–5. https://doi.org/10.1186/s12890-021-01450-5.
[27] Rahman S, Sarker S, Al Miraj MA, Nihal RA, Haque AN, Al Noman A. Deep learning-driven automated detection of COVID-19 from radiography images: a comparative analysis. Cognitive Computation 2021:1–30. https://doi.org/10.1007/s12559-020-09779-5.
[28] Manavalan B, Basith S, Lee G. Comparative analysis of machine learning-based approaches for identifying therapeutic peptides targeting SARS-CoV-2. Brief. Bioinform. 2022;23(1):bbab412. https://doi.org/10.1093/bib/bbab412.
[29] Soszynska-Jozwiak M, Ruszkowska A, Kierzek R, O'Leary CA, Moss WN, Kierzek E. Secondary structure of subgenomic RNA M of SARS-CoV-2. Viruses 2022;14(2):322. https://doi.org/10.3390/v14020322.
[30] Sedik A, Hammad M, Abd El-Samie FE, Gupta BB, Abd El-Latif AA. Efficient deep learning approach for augmented detection of coronavirus disease. Neural Computing and Applications 2022;34:11423–40. https://doi.org/10.1007/s00521-020-05410-8.
[31] Aldhafiri FK. COVID-19 and gut dysbiosis, understanding the role of probiotic supplements in reversing gut dysbiosis and immunity. Nutrition Clinique et Métabolisme 2022;36(3):153–61. https://doi.org/10.1016/j.nupar.2022.01.003.
[32] Alves MHME, Mahnke LC, Macedo TC, dos Santos Silva TK, Junior LBC. The enzymes in COVID-19: a review. Biochimie 2022;197:38–48. https://doi.org/10.1016/j.biochi.2022.01.015.
[33] Chowdhury ME, Rahman T, Khandakar A, Mazhar R, Kadir MA, Mahbub ZB. Can AI help in screening viral and COVID-19 pneumonia? 2020;8:132665–76. https://doi.org/10.1109/ACCESS.2020.3010287.
[34] Joshi S, Parkar J, Ansari A, Vora A, Talwar D, Tiwaskar M, et al. Role of favipiravir in the treatment of COVID-19. Int J Infect Dis 2021;102:501–8. https://doi.org/10.1016/j.ijid.2020.10.069.
[35] Sagris M, Theofilis P, Antonopoulos AS, Oikonomou E, Tsioufis K, Tousoulis D. Genetic predisposition and inflammatory inhibitors in COVID-19: where do we Stand? Biomedicines 2022;10(2):242. https://doi.org/10.3390/biomedicines10020242.
[36] Chidambaranathan-Reghupaty S, Fisher PB, Sarkar D. Hepatocellular carcinoma (HCC): epidemiology, etiology and molecular classification. Adv Cancer Res 2021;149:1–61. https://doi.org/10.1016/bs.acr.2020.10.001.
[37] Viant C, Wirthmiller T, ElTanbouly MA, Chen ST, Cipolla M, Ramos V, et al. Germinal center–dependent and–independent memory B cells produced throughout the immune response. J. Exp. Med. 2021;218(8):e20202489. https://doi.org/10.1084/jem.20202489.
[38] Šušak B, Mikulić V, Lazarević A, Mikulić I, Arapović J. Sustained seroprevalence of SARS-CoV-2 antibodies 1 year after infection: one of the first COVID-19 cluster cases in Bosnia and Herzegovina. Bosn J Basic Med Sci 2022;22(1):147. https://doi.org/10.17305/bjbms.2021.6340.
[39] Bikle DD. Vitamin D regulation of immune function during covid-19. Rev. Endocr. Metab. Disord. 2022;23:279–85. https://doi.org/10.1007/s11154-021-09707-4.
[40] Siripanthong B, Asatryan B, Hanff TC, Chatha SR, Khanji MY, Ricci F, et al. The pathogenesis and long-term consequences of COVID-19 cardiac injury. basic to translational. Science 2022;7(3_Part_1):294–308. https://doi.org/10.1016/j.jacbts.2021.10.011.
[41] Puntmann VO, Carerj ML, Wieters I, Fahim M, Arendt C, Hoffmann J, et al. Outcomes of cardiovascular magnetic resonance imaging in patients recently recovered from coronavirus disease 2019 (COVID-19). JAMA Cardiol 2020;5(11): 1265–73. https://doi.org/10.1001/jamacardio.2020.3557.
[42] Park A, Iwasaki A. Type I and type III interferons–induction, signaling, evasion, and application to combat COVID-19. Cell Host Microbe 2020;27(6):870–8. https://doi.org/10.1016/j.chom.2020.05.008.
[43] Wadman M. Can interferons stop COVID-19 before it takes hold?. 2020. https://doi.org/10.1126/science.369.6500.125.
[44] Chan JFW, Yuan S, Zhang AJ, Poon VKM, Chan CCS, Lee ACY, et al. Surgical mask partition reduces the risk of noncontact transmission in a golden Syrian hamster model for coronavirus disease 2019 (COVID-19). Clin Infect Dis 2020;71(16): 2139–49. https://doi.org/10.1093/cid/ciaa644.
[45] Mar-Cupido R, García V, Rivera G, Sánchez JS. Deep transfer learning for the recognition of types of face masks as a core measure to prevent the transmission of COVID-19. Appl Soft Comput 2022;125:109207. https://doi.org/10.1016/j.asoc.2022.109207.
[46] Yan W, Zheng Y, Zeng X, He B, Cheng W. Structural biology of SARS-CoV-2: open the door for novel therapies. Signal Transduct Target Ther 2022;7(1):26. https://doi.org/10.1038/s41392-022-00884-5.
[47] Su S, Du L, Jiang S. Learning from the past: development of safe and effective COVID-19 vaccines. Nat Rev Microbiol 2021;19(3):211–9. https://doi.org/10.1038/s41579-020-00462-y.
[48] Mahase E. In: Covid-19: Where are we on vaccines and variants?; 2021. 372–n597. https://doi.org/10.1136/bmj.n597.
[49] Caputo V, Calvino G, Strafella C, Termine A, Fabrizio C, Trastulli G, et al. Tracking the initial diffusion of SARS-CoV-2 omicron variant in Italy by RT-PCR and comparison with alpha and Delta variants spreading. Diagnostics 2022;12(2): 467. https://doi.org/10.3390/diagnostics12020467.
[50] Wang C, Han J. Will the COVID-19 pandemic end with the Delta and omicron variants? Environmental Chemistry Letters 2022;20:2215–25. https://doi.org/10.1007/s10311-021-01369-7.
[51] Rössler A, Riepler L, Bante D, von Laer D, Kimpel J. SARS-CoV-2 omicron variant neutralization in serum from vaccinated and convalescent persons. New England Journal of Medicine 2022;386(7):698–700. https://doi.org/10.1056/NEJMc2119236.
[52] Del Rio C, Omer SB, Malani PN. Winter of omicron-the evolving COVID-19 pandemic. JAMA 2022;327(4):319–20. https://doi.org/10.1001/jama.2021.24315.
[53] Effectiveness of Covid-19 vaccines against the B. 1.617. 2 (Delta) variant. Bernal JL, Andrews N, Gower C, Gallagher E, Simmons R, Thelwall S, et al., editors. New England Journal of Medicine 2021;385:585–94. https://doi.org/10.1056/NEJMoa2108891.
[54] Muik A, Lui BG, Wallisch AK, Bacher M, Mühl J, Reinholz J, et al. Neutralization of SARS-CoV-2 omicron by BNT162b2 mRNA vaccine–elicited human sera. Science 2022;375(6581):678–80. https://doi.org/10.1126/science.abn7591.

[55] Abu-Raddad LJ, Chemaitelly H, Coyle P, Malek JA, Ahmed AA, Mohamoud YA, et al. SARS-CoV-2 antibody-positivity protects against reinfection for at least seven months with 95% efficacy. EClinicalMedicine 2021;35:100861. https://doi.org/10.1016/j.eclinm.2021.100861.
[56] La Salvia M, Secco G, Torti E, Florimbi G, Guido L, Lago P, et al. Deep learning and lung ultrasound for Covid-19 pneumonia detection and severity classification. Comput Biol Med 2021;136:104742. https://doi.org/10.1016/j.compbiomed.2021.104742.
[57] Wong PK, Yan T, Wang H, Chan IN, Wang J, Li Y, et al. Automatic detection of multiple types of pneumonia: open dataset and a multi-scale attention network. Biomedical Signal Processing and Control 2022;73:103415. https://doi.org/10.1016/j.bspc.2021.103415.
[58] Bashar A, Latif G, Ben Brahim G, Mohammad N, Alghazo J. COVID-19 pneumonia detection using optimized deep learning techniques. Diagnostics 2021;11(11):1972. https://doi.org/10.3390/diagnostics11111972.
[59] Singh RK, Pandey R, Babu RN. COVIDScreen: explainable deep learning framework for differential diagnosis of COVID-19 using chest X-rays. Neural Computing and Applications 2021;33(14):8871–92. https://doi.org/10.1007/s00521-020-05636-6.
[60] Shelke A, Inamdar M, Shah V, Tiwari A, Hussain A, Chafekar T, Mehendale N. Chest X-ray classification using deep learning for automated COVID-19 screening. SN Comput. Sci. 2021;2(4):1–9. https://doi.org/10.1007/s42979-021-00695-5.
[61] Chaunzwa TL, Hosny A, Xu Y, Shafer A, Diao N, Lanuti M, et al. Deep learning classification of lung cancer histology using CT images. Sci Rep 2021;11:5471. https://doi.org/10.1038/s41598-021-84630-x.
[62] Mazoure B, Mazoure A, Bédard J, Makarenkov V. DUNEScan: a web server for uncertainty estimation in skin cancer detection with deep neural networks. Sci Rep 2022;12:179. https://doi.org/10.1038/s41598-021-03889-2.
[63] Alanazi MF, Ali MU, Hussain SJ, Zafar A, Mohatram M, Irfan M, et al. Brain Tumor/Mass classification framework using magnetic-resonance-imaging-based isolated and developed transfer deep-learning model. Sensors 2022;22(1):372. https://doi.org/10.3390/s22010372.
[64] Ho C, Zhao Z, Chen XF, Sauer J, Saraf SA, Jialdasani R, et al. A promising deep learning-assistive algorithm for histopathological screening of colorectal cancer. Sci Rep 2022;12:2222. https://doi.org/10.1038/s41598-022-06264-x.
[65] Qi A, Zhao D, Yu F, Heidari AA, Wu Z, Cai Z, et al. Directional mutation and crossover boosted ant colony optimization with application to COVID-19 X-ray image segmentation. Comput Biol Med 2022;148:105810. https://doi.org/10.1016/j.compbiomed.2022.105810.
[66] Ouchicha C, Ammor O, Meknassi M. CVDNet: a novel deep learning architecture for detection of coronavirus (Covid-19) from chest x-ray images. Chaos, Solitons & Fractals 2020;140:110245. https://doi.org/10.1016/j.chaos.2020.110245.
[67] Sahin ME. Deep learning-based approach for detecting COVID-19 in chest X-rays. Biomedical Signal Processing and Control 2022;78:103977. https://doi.org/10.1016/j.bspc.2022.103977.
[68] Mukherjee H, Ghosh S, Dhar A, Obaidullah SM, Santosh KC, Roy K. Deep neural network to detect COVID-19: one architecture for both CT scans and chest X-rays. Applied Intelligence 2021;51(5):2777–89. https://doi.org/10.1007/s10489-020-01943-6.
[69] Tangudu V, Kakarla J, Venkateswarlu IB. COVID-19 detection from chest x-ray using MobileNet and residual separable convolution block. Soft Computing 2022;26(5):2197–208. https://doi.org/10.1007/s00500-021-06579-3.
[70] Li P, Tang H, Yu J, Song W. LSTM and multiple CNNs based event image classification. Multimed Tools Appl 2021;80(20):30743–60. https://doi.org/10.1007/s11042-020-10165-4.
[71] Tahir AM, Qiblawey Y, Khandakar A, Rahman T, Khurshid U, Musharavati F, et al. Deep learning for reliable classification of COVID-19, MERS, and SARS from chest X-ray images. Cognitive Computation 2022;14:1752–72. https://doi.org/10.1007/s12559-021-09955-1.
[72] Khan E, Rehman MZU, Ahmed F, Alfouzan FA, Alzahrani NM, Ahmad J. Chest X-ray classification for the detection of COVID-19 using deep learning techniques. Sensors 2022;22(3):1211. https://doi.org/10.3390/s22031211.
[73] Chouat I, Echtioui A, Khemakhem R, Zouch W, Ghorbel M, Hamida AB. COVID-19 detection in CT and CXR images using deep learning models. Biogerontology 2022;23:65–84. https://doi.org/10.1007/s10522-021-09946-7.
[74] Kundu R, Singh PK, Ferrara M, Ahmadian A, Sarkar R. ET-NET: an ensemble of transfer learning models for prediction of COVID-19 infection through chest CT-scan images. Multimed Tools Appl 2022;81(1):31–50. https://doi.org/10.1007/s11042-021-11319-8.
[75] Wang L, Lin ZQ, Wong A. Covid-net: a tailored deep convolutional neural network design for detection of covid-19 cases from chest x-ray images. Sci Rep 2020;10:19549. https://doi.org/10.1038/s41598-020-76550-z.
[76] Cohen JP, Morrison P, Dao L. COVID-19 image data collection. arXiv preprint. 2020. https://doi.org/10.48550/arXiv.2003.11597.
[77] Kumar A, Tripathi AR, Satapathy SC, Zhang YD. SARS-net: COVID-19 detection from chest x-rays by combining graph convolutional network and convolutional neural network. Pattern Recognition 2022;122:108255. https://doi.org/10.1016/j.patcog.2021.108255.
[78] Abbas A, Abdelsamea MM, Gaber MM. Classification of COVID-19 in chest X-ray images using DeTraC deep convolutional neural network. Applied Intelligence 2021;51(2):854–64. https://doi.org/10.1007/s10489-020-01829-7.
[79] Li L, Qin L, Xu Z, Yin Y, Wang X, Kong B, et al. Using artificial intelligence to detect COVID-19 and community-acquired pneumonia based on pulmonary CT: evaluation of the diagnostic accuracy. Radiology 2022;296(2):E65–71. https://doi.org/10.1148/radiol.2020200905.
[80] Mansour RF, Escorcia-Gutierrez J, Gamarra M, Gupta D, Castillo O, Kumar S. Unsupervised deep learning based variational autoencoder model for COVID-19 diagnosis and classification. Pattern Recognition Letters 2021;151:267–74. https://doi.org/10.1016/j.patrec.2021.08.018.
[81] Ragab M, Alshehri S, Alhakamy NA, Mansour RF, Koundal D. Multiclass classification of chest X-ray images for the prediction of COVID-19 using capsule network. Comput Intell Neurosci 2022;2022:6185013. https://doi.org/10.1155/2022/6185013.
[82] He K, Zhang X, Ren S, Sun J. Deep residual learning for image recognition. In Proceedings of the IEEE conference on computer vision and pattern recognition 2016:770–8. https://doi.org/10.1109/CVPR.2016.90.
[83] Huang G, Liu Z, Van Der Maaten L, Weinberger KQ. Densely connected convolutional networks. In Proceedings of the IEEE conference on computer vision and pattern recognition 2017:4700–8. https://doi.org/10.1109/CVPR.2017.243.
[84] Hochreiter S, Schmidhuber J. Long short-term memory. Neural Comput 1997;9(8):1735–80. https://doi.org/10.1162/neco.1997.9.8.1735.
[85] Mo Z, Luo D, Wen T, Cheng Y, Li X. FPGA implementation for odor identification with depthwise separable convolutional neural network. Sensors 2021;21(3):832. https://doi.org/10.3390/s21030832.
[86] Yan T, Wong PK, Ren H, Wang H, Wang J, Li Y. Automatic distinction between COVID-19 and common pneumonia using multi-scale convolutional neural network on chest CT scans. Chaos, Solitons & Fractals 2020;140:110153. https://doi.org/10.1016/j.chaos.2020.110153.
[87] Rahman T, Khandakar A, Qiblawey Y, Tahir A, Kiranyaz S, Kashem SBA, et al. Exploring the effect of image enhancement techniques on COVID-19 detection using chest X-ray images. Comput Biol Med 2021;132:104319. https://doi.org/10.1016/j.compbiomed.2021.104319.
[88] Kermany D, Zhang K, Goldbaum M. Labeled optical coherence tomography (oct) and chest x-ray images for classification. Mendeley data 2018;2(2). https://doi.org/10.17632/rscbjbr9sj.2.
[89] Szegedy C, Ioffe S, Vanhoucke V, Alemi AA. Inception-v4, inception-resnet and the impact of residual connections on learning. Proceedings of the AAAI Conference on Artificial Intelligence 2017;31(1):4278–84. https://doi.org/10.1609/aaai.v31i1.11231.
[90] Szegedy C, Vanhoucke V, Ioffe S, Shlens J, Wojna Z. Rethinking the inception architecture for computer vision. In Proceedings of the IEEE conference on computer vision and pattern recognition; 2016:2818–26. https://doi.org/10.1109/CVPR.2016.308.
[91] Howard AG, Zhu M, Chen B, Kalenichenko D, Wang W, Weyand T. Mobilenets: Efficient convolutional neural networks for mobile vision applications. 2017. https://doi.org/10.48550/arXiv.1704.04861.
[92] Zoph B, Vasudevan V, Shlens J, Le QV. Learning transferable architectures for scalable image recognition. In Proceedings of the IEEE conference on computer vision and pattern recognition 2018:8697–710. https://doi.org/10.1109/CVPR.2018.00907.
[93] Tan M, Le Q. Efficientnet: rethinking model scaling for convolutional neural networks. In: International conference on machine learning. PMLR; 2019. p. 6105–14.
[94] Kingma DP, Ba J. Adam: A method for stochastic optimization. 2014. https://doi.org/10.48550/arXiv.1412.6980. arXiv preprint.
[95] Chandra TB, Verma K, Singh BK, Jain D, Netam SS. Coronavirus disease (COVID-19) detection in chest X-ray images using majority voting based classifier ensemble. Expert systems with applications 2021;165:113909. https://doi.org/10.1016/j.eswa.2020.113909.
[96] Gayathri JL, Abraham B, Sujarani MS, Nair MS. A computer-aided diagnosis system for the classification of COVID-19 and non-COVID-19 pneumonia on chest X-ray images by integrating CNN with sparse autoencoder and feed forward neural network. Comput Biol Med 2022;141:105134. https://doi.org/10.1016/j.compbiomed.2021.105134.
[97] Loey M, El-Sappagh S, Mirjalili S. Bayesian-based optimized deep learning model to detect COVID-19 patients using chest X-ray image data. Comput Biol Med 2022;142:105213. https://doi.org/10.1016/j.compbiomed.2022.105213.
[98] Li C, Yang Y, Liang H, Wu B. Transfer learning for establishment of recognition of COVID-19 on CT imaging using small-sized training datasets. Knowledge-Based Systems 2021;218:106849. https://doi.org/10.1016/j.knosys.2021.106849.
[99] Douaud G, Lee S, Alfaro-Almagro F, Arthofer C, Wang C, McCarthy P, et al. SARS-CoV-2 is associated with changes in brain structure in UK biobank. Nature 2022;604(7907):697–707. https://doi.org/10.1038/s41586-022-04569-5.
[100] Lei F, Liu X, Dai Q, Ling BWK. Shallow convolutional neural network for image classification. SN Appl. Sci. 2020;2:97. https://doi.org/10.1007/s42452-019-1903-4.